

POSTDEADLINE PAPERS

1 9 9 5

INTEGRATED PHOTONICS RESEARCH

FEBRUARY 23-25, 1995

DANA POINT, CALIFORNIA

1995 TECHNICAL DIGEST SERIES
VOLUME 7



SPONSORED BY
OPTICAL SOCIETY OF AMERICA

DISTRIBUTION STATEMENT A

Approved for public release;
Distribution Unlimited

DTIC QUALITY INSPECTED 6

19960325 098

INTEGRATED PHOTONICS RESEARCH
POSTDEADLINE PAPERS
FEBRUARY 24, 1995
7:00pm Salon I

PD1

7:00-7:12pm

Avalanche Gain in $\text{InAs}_{1-y}\text{P}_y$ Photodetectors for Mid-IR Focal Plane Arrays

D. S. Kim, S. R. Forrest, *Princeton University*, G. H. Olsen, M. J. Lange, *Sensors Unlimited, Inc.*, R. U. Martinelli, N. J. Di Giuseppe, *David Sarnoff Research Center*

PD2

7:12-7:24pm

An 8 Channel Digitally Tunable Transmitter

C. H. Joyner, M. Zirngibl, J. C. Centanni, *AT&T Bell Laboratories*

PD3

7:24-7:36pm

8 x 2nm Polarization-Independent WDM Detector Based on Compact Arrayed Waveguide Demultiplexer

M. R. Amersfoot, J. B. D. Soole, H.P. LeBlanc, N. C. Andreadakis, A. Rajhel, C. Caneau, *Bellcore*

PD4

7:36-7:48pm

Packaged Zero-Loss Polarization-Independent Four-Channel Multi-Grating Filter

Jean-Pierre Weber, *Ericsson Components AB, Fiber Optics Research Center Sweden*, Bjorn Stoltz, Marie Dasler, *Ericsson Components AB, Opto and RF Power Products, Sweden*

PD5

7:48-8:00pm

Observation of Modulated Crosstalk in Multichannel Acoustooptic Switches

Janet Lehr Jackel, Jane E. Baran, *Bellcore*, David A. Smith, Rohini S. Chakravarthy, *Case Western Reserve University*, Daniel J. Fritz, *United Technologies Research Center*

PD6

8:00-8:12pm

Acoustic Pulse Measurements of Acousto-Optic Tunable Filter Properties

L. B. Aronson, G. Rankin, T. R. Ranganath, D. W. Dolfi, *Hewlett Packard Laboratories*



PD7

8:12-8:24pm

Basic Design Rule of 1.3- μ m InP-Based Strained MQW Lasers for High Temperature Operation

S. Seki, H. Oohashi, H. Sugiura, T. Hirono, K. Yokoyama, *NTT Opto-electronics Laboratories, Japan*

PD8

8:24-8:36pm

The Application of the Alternating Directional Vector Beam Propagation Method to Semiconductor Rib Waveguide Y-Junctions

Jun Yu, Bell Northern Research Ltd., Canada, David Yevick, Queens University, Canada, Witold Bardyszewski, Warsaw University, Poland

PD9

8:36-8:48pm

Ball Lens Reflections by Direct Solution of Maxwell's Equations

R. P. Ratowsky, L. Yang, R. J. Deri, J. S. Kallman, Lawrence Livermore National Laboratory, G. Trott, Hewlett-Packard Laboratories

Avalanche Gain in $\text{InAs}_y\text{P}_{1-y}$ Photodetectors for Mid-IR Focal Plane Arrays

D. S. Kim and S. R. Forrest
Advanced Technology Center for Photonics and Optoelectronic Materials
Department of Electrical Engineering
Princeton University
Princeton, NJ 08544

G. H. Olsen and M. J. Lange
Sensors Unlimited, Inc.
3490 US Route 1, Bldg. 12
Princeton, NJ 08540

R. U. Martinelli and N. J. Di Giuseppe
David Sarnoff Research Center
Princeton, NJ 08540

Abstract

Avalanche gains >80 are observed in $\text{InAs}_y\text{P}_{1-y}$ ($0.1 < y < 0.3$) grown on p-type InP substrates with lattice strains $\leq 1\%$. The devices have a primary dark current ≥ 200 pA. The $\text{InAs}_y\text{P}_{1-y}$ layers have the same lattice parameter as compositions of $\text{In}_x\text{Ga}_{1-x}\text{As}$ which absorb wavelengths $\leq 2.1\mu\text{m}$, for use in avalanche photodiode imaging arrays operating in the mid-IR spectral range.

Avalanche Gain in $\text{InAs}_y\text{P}_{1-y}$ Photodetectors for Mid-IR Focal Plane Arrays

D. S. Kim, S. R. Forrest, G. H. Olsen[@], M. J. Lange[@], R. U. Martinelli[#] and N. J. Di Giuseppe[#]

Advanced Technology Center for Photonics and Optoelectronic Materials
Princeton University
Princeton, NJ 08544

Very high performance, integrated focal plane arrays for use in imaging applications have been demonstrated using lattice-matched $\text{In}_{0.53}\text{Ga}_{0.47}\text{As}/\text{InP}$ p-i-n photodiodes as the detection element. Unfortunately, these devices are sensitive only to wavelengths, $\lambda < 1.7\mu\text{m}$, limiting their utility for many moisture sensing, LIDAR and thermal measurement applications. More recently, we have demonstrated integrated "three-color" detectors employing $\text{In}_x\text{Ga}_{1-x}\text{As}$ ($x \geq 0.53$) photodiode arrays which have optical sensitivity to $\lambda = 2.6\mu\text{m}$ [1]. For very low signal levels, it is useful, however, to extend the sensitivity obtained using a simple p-i-n detector. One possibility for increasing long wavelength focal plane sensitivity is to use avalanche photodiodes (APDs). In this work, we describe initial success in the effort to develop such a device. We report the observation of large avalanche gains (40-80) in the presence of small primary dark currents (~ 500 pA at 90% of the breakdown voltage, V_B) in $\text{InAs}_y\text{P}_{1-y}$, where $0.1 < y < 0.3$ was chosen to make this material lattice-matched to narrow band gap ($\sim 0.5\text{eV}$) $\text{In}_x\text{Ga}_{1-x}\text{As}$ ($0.6 < x < 0.7$). These results represent the first significant step in realizing APDs for integrated focal plane arrays useful in the mid-IR wavelength region.

The device structure to be used for mid-IR detection is shown schematically in Fig. 1a. The structure is a separate absorption and multiplication region APD (or SAM-APD) which has proven effective in eliminating tunneling leakage current that occurs in narrow band gap semiconductors such as $\text{In}_{0.53}\text{Ga}_{0.47}\text{As}$ when in the presence of the high applied electric fields required for avalanche multiplication. To make such a device sensitive to $\lambda > 1.65\mu\text{m}$, additional In must be added to $\text{In}_x\text{Ga}_{1-x}\text{As}$. Since this results in an increase in the lattice constant, this material is no longer lattice-matched to the large band gap InP. Lattice-mismatch generates misfit dislocations at the interface between the contacting layers, which act as recombination centers that increase dark current, and serve as nucleation sites for microplasmas. To circumvent this problem, As is added to the InP multiplication region, such that $\text{InAs}_y\text{P}_{1-y}$ serves as the large band gap material. The As concentration is chosen such that this layer will ultimately have the same lattice constant as the absorbing $\text{In}_x\text{Ga}_{1-x}\text{As}$. In this way, dislocations are confined to the mismatched InP/ $\text{InAs}_y\text{P}_{1-y}$ interface, while being minimized at the lattice-matched $\text{InAs}_y\text{P}_{1-y}/\text{In}_x\text{Ga}_{1-x}\text{As}$ heterojunction.

To determine the gain characteristics of $\text{InAs}_y\text{P}_{1-y}$, the structure in Fig. 1b was fabricated. Undoped, $3\mu\text{m}$ thick $n^-\text{-InAs}_y\text{P}_{1-y}$ was grown by MOCVD directly onto a p-type, Zn:InP substrate. During growth at 700°C , Zn from the highly doped ($> 5 \times 10^{18} \text{ cm}^{-3}$) substrate diffuses into the $\text{InAs}_y\text{P}_{1-y}$ layer, forming the p-n junction. This places the p-n junction (which is the location of the highest electric fields) beyond the extent of the misfit dislocations that form at the $\text{InAs}_y\text{P}_{1-y}/\text{InP}$ heterojunction. Similar results are obtained for devices grown by hydride vapor phase epitaxy. Following growth, a $50\mu\text{m}$ diameter Au:Ge:Au n-contact was deposited onto the surface of an approximately $150\mu\text{m}$ diameter mesa structure, formed by etching in 1% Br:MeOH. Contact alloying was achieved by rapid thermal annealing.

Three wafers were grown and tested for this study, with their parameters listed in Table 1. In the far right-hand column of the Table is shown the cut-off wavelength of the composition of $\text{In}_x\text{Ga}_{1-x}\text{As}$ lattice-matched to $\text{In}_y\text{As}_{1-y}\text{P}$ in the adjacent column. To measure gain, the devices were

[@] Address: Sensors Unlimited, Inc., 3490 US Route 1, Princeton, NJ 08540

[#] Address: David Sarnoff Research Center, Princeton, NJ 08540

illuminated from the top surface using 633 nm light from a He:Ne laser, or from the bottom surface using 1064nm light from a Nd-YAG laser. The InP substrate is transparent to the 1064nm radiation. Light was introduced using a single mode fiber scanned from edge to edge of the mesa to ensure that the gain of the devices was uniform. Since the 633nm light is strongly adsorbed at the $\text{InAs}_y\text{P}_{1-y}$ surface, a measurement of gain due to top illumination yields the hole multiplication factor, M_p . Similarly, illumination through the substrate side provides the electron multiplication factor, M_n .

The dark-current is relatively voltage independent at $V < 25\text{V}$, increasing monotonically toward breakdown at voltages greater than 40V. Primary dark currents as low as 200 pA for wafer A are observed at $0.5V_B = 25\text{V}$, whereas the more highly strained, lower band gap wafer C has a dark current of 100 nA at this same voltage. In the case of wafer A, the dark current increases to only 1nA at $0.9V_B$. These results suggest that the dark current is increasing primarily as a result of avalanche gain rather than the result of parasitic effects such as edge breakdown or tunneling. The photocurrent and multiplication characteristics of the wafer C are shown in Fig 2. The photocurrent remains constant until approximately $0.6V_B$, at which point M increases toward its maximum value at V_B . From these data, we observe that gains as high as 70 - 80 are obtained for wafers B and C, and from 30 to 40 for wafer A. Similarly, at all voltages and for all wafers, we find that $M_p \approx M_n$. Variations in both the maximum values of M , and between M_n and M_p from wafer to wafer are not significant.

The electric fields at breakdown are measured to be $1\text{-}1.5 \times 10^5$ V/cm, or roughly four times smaller than is required in conventional, III-V based APD materials such as InP. The probable origin of the secondary carriers is ionization of the deep levels arising from the misfit defects, which would also account for the nearly equal values obtained for both M_n and M_p in these diodes. To test this conclusion, we also measured the gain as a function of light intensity for 633nm wavelength light incident via the top surface (Fig. 3). The gain is a strong function of light intensity, with M_p at 46V decreasing from a maximum value of 40 at an input power of 350 nW, to only 9 at 6 μW . This is consistent with the hypothesis that gain occurs via the ionization of a limited number of defect states. Hence, the gain decreases at relatively high input power levels where a large fraction of the defects are ionized at any given time.

Preliminary results for a full SAM-APD structure operating in the mid-IR range will be presented.

In conclusion, we have demonstrated that low primary dark currents and high avalanche gains can be achieved in lattice-mismatched $\text{InAs}_y\text{P}_{1-y}$ ($0.1 < y < 0.3$) grown without compositional grading on p-type InP substrates, where the $\text{InAs}_y\text{P}_{1-y}$ strain is as high as 1%. This range of $\text{InAs}_y\text{P}_{1-y}$ material is lattice-matched to $\text{In}_x\text{Ga}_{1-x}\text{As}$ ($0.6 < x < 0.7$), which can absorb light at wavelengths as long as 2.1 μm . Hence, these results strongly suggest that $\text{InAs}_y\text{P}_{1-y}$ can be used as the multiplication layer in SAM-APD imaging arrays for sensing applications in the mid-IR. We have also found that the ionization coefficients of electrons and holes are approximately equal in the compositions of $\text{InAs}_y\text{P}_{1-y}$, and over the range of electric fields investigated.

The authors acknowledge the support of Ballistic Missile Defense Organization and the Office of Naval Research (A. M. Goodman and Y. S. Park).

Table 1: Parameters of $\text{InAs}_y\text{P}_{1-y}$ Wafers

Wafer ID	y	lattice parameter (Å)	strain (%)	λ_g ; $\text{InAs}_y\text{P}_{1-y}$ (μm)	λ_g ; $\text{InGa}_x\text{As}_{1-x}$ (μm)
A	0.12	5.8947	-0.43	1.02	1.87
B	0.25	5.9199	-0.71	1.15	2.04
C	0.29	5.9267	-0.97	1.20	2.11

[1] D. S. Kim, S. R. Forrest, M.J. Lange, G. H. Olsen and M. J. Cohen, Photonic Tech. Lett. **6**, 235 (1994).

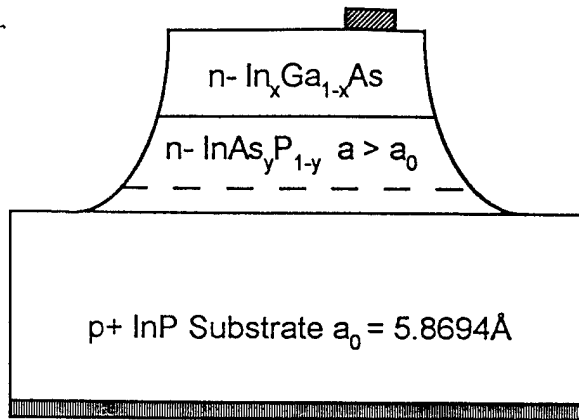


Fig. 1a

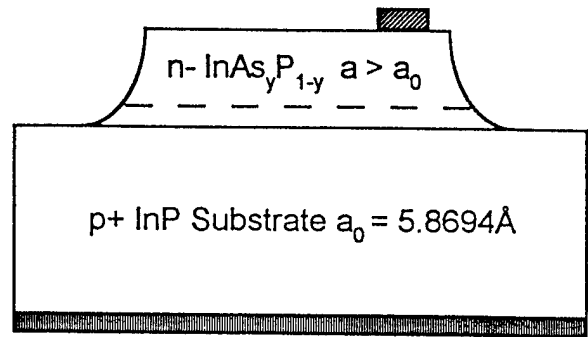


Fig.1b

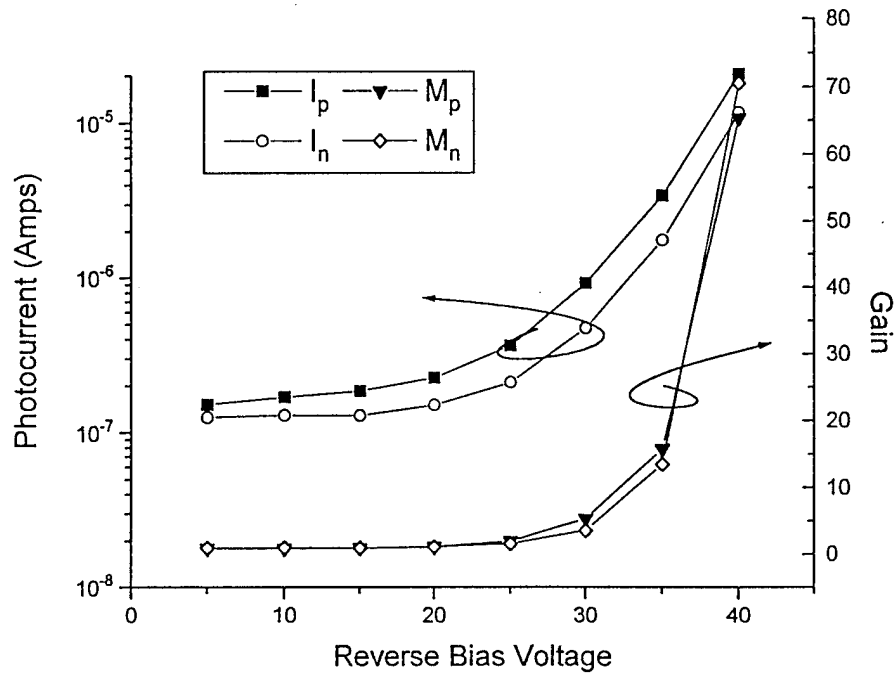


Fig. 2

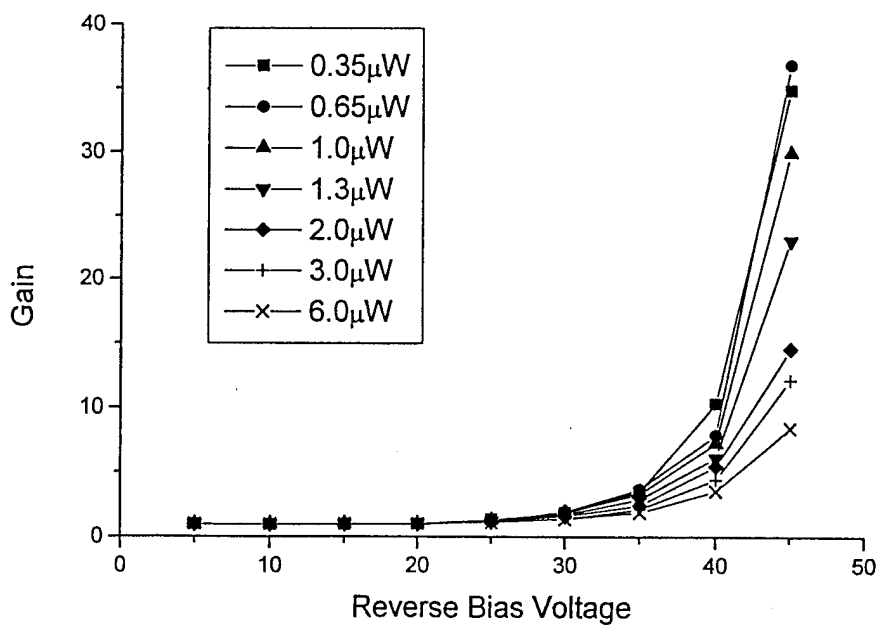


Fig. 3

An 8 Channel Digitally Tunable Transmitter

C.H. Joyner, M. Zirngibl and J.C. Centanni
AT&T Bell Laboratories
Crawford Hill Laboratory
Holmdel, NJ 07733

Abstract:

We demonstrate an 8 frequency (1.567 to 1.580 μm) digitally tunable laser based on a waveguide grating router with an electroabsorption modulated (-10dB/V) output. A unique output coupler design delivers an ASE noise suppression of -55 dB/Å.

An 8 Channel Digitally Tunable Transmitter with Electroabsorption Modulated Output by Selective Area Epitaxy

C.H. Joyner, M. Zirngibl and J.C. Centanni
AT&T Bell Laboratories
Crawford Hill Laboratory
Holmdel, NJ 07733

I. INTRODUCTION

Wavelength-division-multiplexed (WDM) lightwave communication systems are receiving increasing attention for long distance as well as local applications. Many such multi-frequency lasers have been proposed [1-4], but few have been integrated with modulators to become transmitters. In this paper we present an integrated WDM transmitter with precise channel spacings in which any of 8 wavelengths may be selected and modulated at a single output port.

II. DESIGN AND FABRICATION

A schematic diagram of the transmitter is shown in figure 1. The laser cavity is similar to our previously reported design [5]. The novel feature of the current design arises from the realization that light emerging from the waveguide grating arms radiates into first order and second order grating modes. The primary mode is always aligned with the amplifier completing the left side of the laser cavity, while the secondary mode represented an unwanted loss in past designs. In the new design, the free space region now includes an output port that captures second order diffracted light from the waveguide grating (ref. M. Zirngibl, "Wavelength grating router with output couplers", U.S. patent application). This port serves as an output coupler from the main lasing cavity without increasing the loss of the lasing cavity. The output port is coupled to an on-chip electroadsorption modulator that is terminated on an AR coated facet. The cross-section of our device is shown in figure 2. It is similar to our previously reported structure [6], except that the laser active region and modulator are grown by selective area epitaxy (SAE).

III. RESULTS and DISCUSSION

The device was tested under DC conditions in chip form. With cleaved facets, the laser had a cw threshold of 60-70 mA with this current split equally between the amplifiers at either end of the cavity. The output power measured directly at the left cleaved laser facet was -10 dBm into a lensed single mode fiber, with an applied current of 100 mA. The power from the modulator port was -16 dBm under the same conditions. The modulator gave an extinction ratio of -10 dB/V at a bias of -5V. Passive waveguide tests with the amplifiers removed indicate that the coupling to the modulator port is approximately -4 dB. The upper half of Figure 3 shows spectra in which each of the channels was powered separately, monitored at the modulator facet, and superimposed. The relative channel spacing is extremely precise. Note, however, that channels 1 and 8 also have significant power in the next free spectral range of the router. The lower half of figure 3 shows the output of channel 5 observed through the modulator port on a more sensitive power scale with 1 Å bandwidth

resolution. Note that the amplified spontaneous emission (ASE) noise is suppressed by -55dB when measured with 1 Å resolution, which shows another advantage of our output coupler design. The signal is filtered by one additional pass through the router before it reaches the modulator. If the output fiber were coupled to the amplifier port, noise suppression would typically be only -40 dB / Å. The contributions from other pass bands of the router, seen left and right of the main peak, are generally down by -35dB for channels 2 through 7.

The reason for the anomalous behavior of channels 1 and 8 is the nature of the SAE mask used to create the band gap shifts. SAE is sensitive to the filling factor (ratio of area masked to that unmasked) in the immediate vicinity of the unmasked region undergoing epitaxial growth. The amplifiers for channels 1 and 8 were at either outer edge of the amplifier array. Thus, seeing neighbors on only one side, they experienced less of an increase in quantum well thickness and therefore a shorter wavelength bandgap. The main determining factor in the selection of which bandpass the cavity will lase upon is the peak of the ASE gain spectrum. This difficulty can be easily overcome by using dummy amplifier sections flanking the outermost ones.

IV. CONCLUSIONS

We have demonstrated an 8 frequency digitally tunable laser based on a waveguide grating router with an electroabsorption modulated output. The channel wavelengths range from 1.567 to 1.580 μm, useful for WDM communications networks. The channel spacings of (1.6nm) 200 GHz are extremely precise. The DC modulator extinction ratio is -10 dB/V with a -5V bias. A unique output coupler design delivers an ASE noise suppression of -55 dB/Å.

REFERENCES

- 1) K.R. Pouguntke, J.B. Soole, A. Scherer, H.P. LeBlanc, R. Bhat and M.A. Koza "Simultaneous Multiple Wavelength Operation of a Multiple Array Grating Integrated Cavity Laser", Appl. Phys. Lett. Vol. 62, pp. 2034-2036, 1993.
- 2) R.C. Alferness, U. Koren, B.I. Miller, M.G. Young, T.L. Koch, G. Raybon, and C.A. Burrus, "Broadly tunable InGaAsP/InP laser based on a vertical directional coupler with 75nm tuning range", Appl. Phys. Lett., 1992, vol. 60, pp. 3209-3211.
- 3) V. Jayaraman, M.E. Heimbuch, L.A. Coldren and S.P. DenBaars, "Widely tunable continuous-wave InGaAsP/InP sampled grating lasers", Electron. Lett., vol. 4, pp. 1492-1494, 1994.
- 4) M.G. Young, U. Koren, B.I. Miller, M.A. Newkirk, M. Chien, M. Zirngibl, C. Dragone, B. Tell, H.M. Presby, and Greg Raybon "A 16 X 1 Wavelength Division Multiplexer with Integrated Distributed Bragg Reflector Lasers and Electroabsorption Modulators", Photon. Technol. Lett., vol. 5, pp. 908-910, 1993.
- 5) M. Zirngibl and C.H. Joyner, "A 12-Frequency WDM Laser Based on a Transmissive Waveguide Grating Router", Electron. Lett., vol. 30., pp. 700-701, 1994.
- 6) C.H. Joyner, M. Zirngibl, and J.P. Meester, "A Multifrequency Waveguide Grating Laser by Selective Area Epitaxy", Photon. Technol. Lett., vol. 6, pp. 1277-1279, 1994.

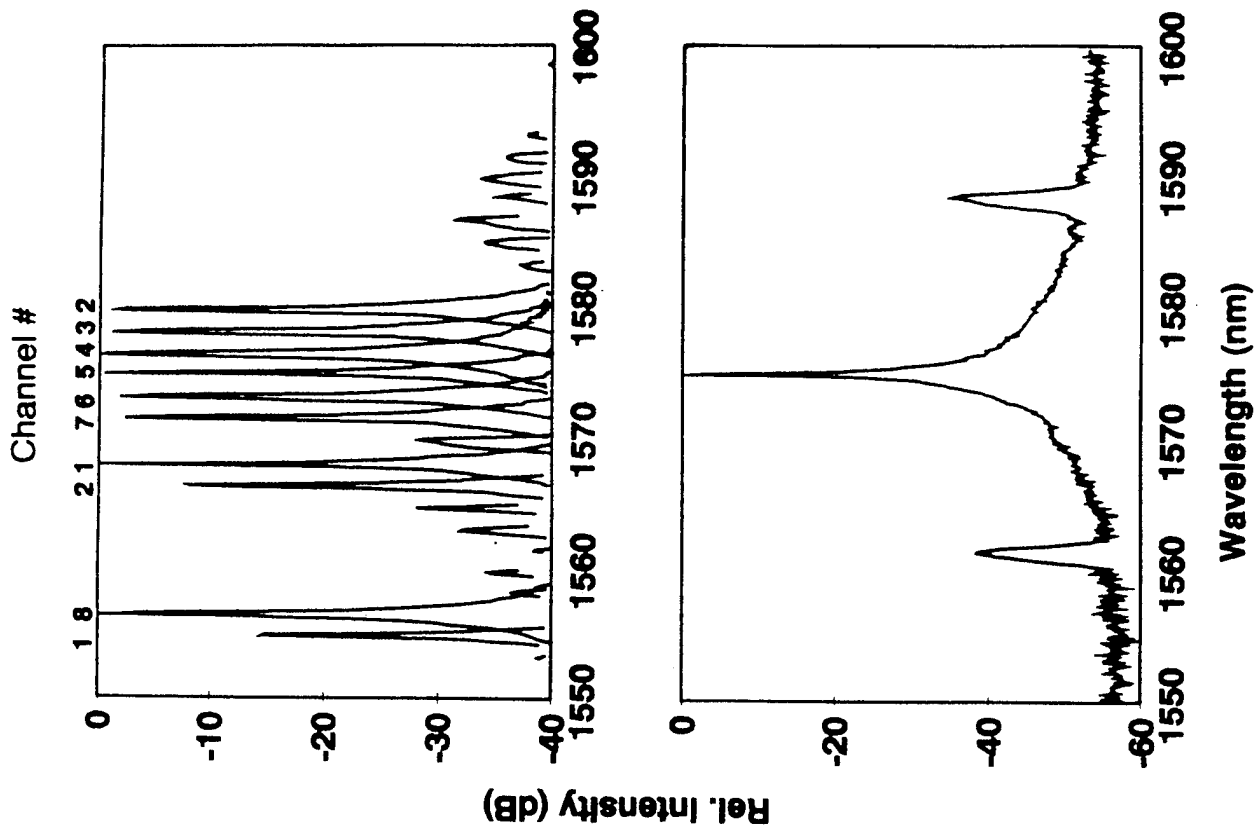


FIGURE 3.

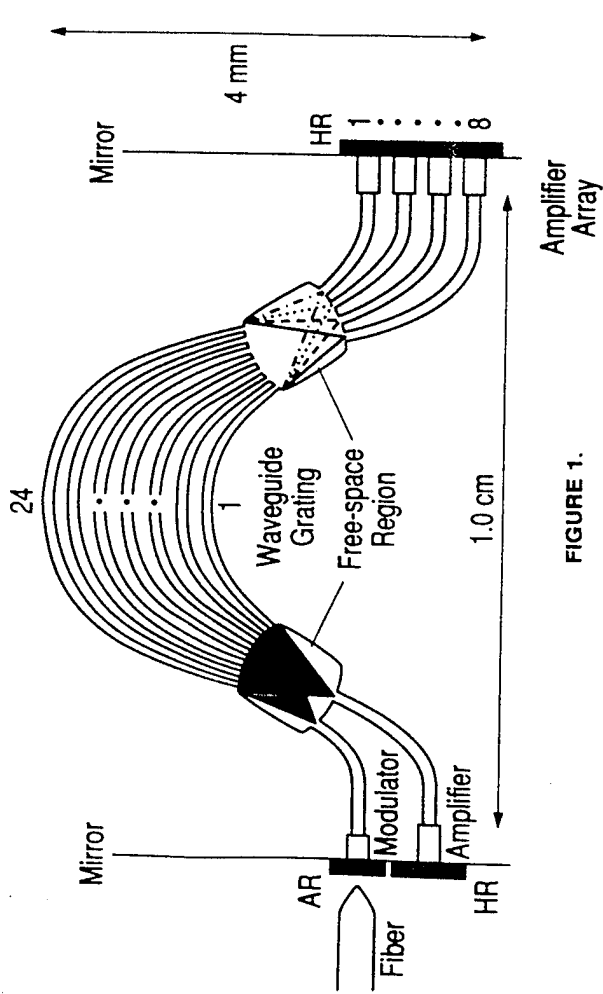


FIGURE 1.

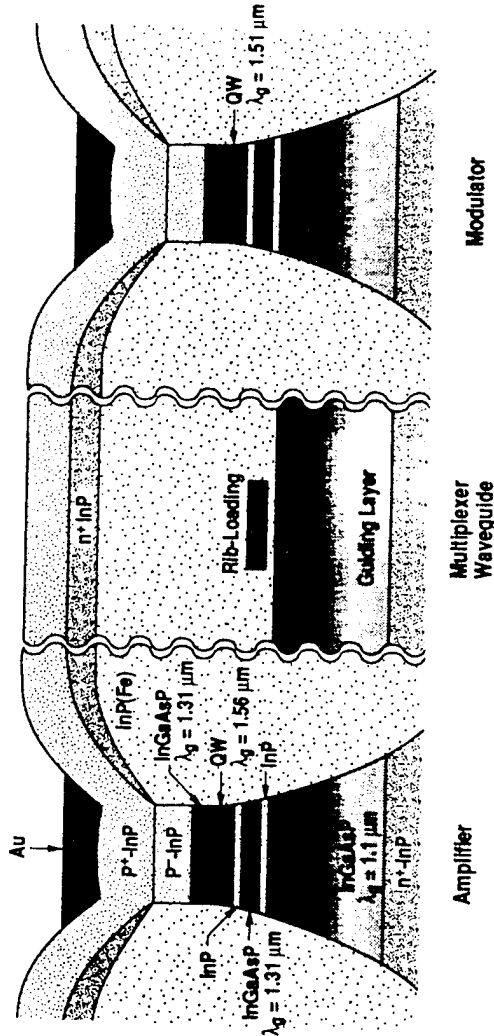


FIGURE 2.

8 x 2nm Polarization-Independent WDM Detector Based on Compact Arrayed Waveguide Demultiplexer

M.R.Amersfoort, J.B.D.SooLe, H.P.LeBlanc, N.C.Andreadakis, A.Rajhel, and C.Caneau,
Bellcore, 331 Newman Springs Road, Red Bank, NJ 07701

Abstract

We report the first polarization-independent monolithic WDM detector. 8 x 2nm channels, from 1.544 μ m to 1.558 μ m wavelength, were demultiplexed and detected by the compact 3.7mm x 4.0mm device without measurable polarization-sensitivity.

Summary

Introduction:

Multiple-wavelength detection is needed for emerging wavelength division multiplexed (WDM) fiber networks. One approach being researched is the integration of the wavelength demultiplexing and detection functions onto a single chip of InP-based material. This avoids the problem of connecting an array of fibers to detectors and allows the possibility of monolithic integration of array amplifiers to form a single-chip WDM receiver. High-speed detection using small area waveguide detectors is also readily achievable [1].

One of the most significant impediments to this approach, however, is that InP-based wavelength demultiplexers are generally birefringent, dispersing TE and TM signals differently. The InP-based WDM detectors reported to date, based on either planar reflection grating demultiplexers [2, 3] or arrayed waveguide demultiplexers [4, 5], have had TE - TM signal separations ranging from 0.6 to 2.6 times the channel spacing. This is clearly unacceptable for most fiber systems, where the polarization state of the input light is undetermined.

In this paper we report, for the first time, a polarization-independent InP-based WDM detector. It is based on an arrayed waveguide demultiplexer that employs raised-stripe waveguides designed to be free of modal birefringence. We have integrated this with an array of waveguide p-i-n diodes and demonstrate polarization-independent detection for 8 channels separated by 2nm.

Design and fabrication:

The array demultiplexer employed InGaAsP($E_g=1.0\mu$ m) raised-stripe guides on InP. Calculation indicated that 1.9 μ m thickness and 3 μ m stripe-widths give $n(TE)=n(TM)$. A compact 3.7mm x 2.6mm demultiplexer was designed integrated with detectors employing the "hybrid" vertical / butt-coupled scheme [1]. A diagram of the guide and detectors structures is given in Figure 1. Detector layout is shown in Figure 2. The die size of the detector was 3.7mm x 4.0mm.

The layer structure was grown by LP-OMCVD. First, the detector layers (1.0 μ m InGaAs absorption layer; 0.6 μ m p-1.3Q/p-InGaAs contact layer) were grown on n-InP, above an 0.6 μ m-thick n-doped portion of the 1.0Q waveguide layer. Following mesa-definition of the detectors, a further 1.3 μ m of s.i.-1.0Q was grown to complete the waveguiding layer and provide isolation. Waveguide stripes were then etched by H_2/CH_4 R.I.E., $\sim 0.2\mu$ m into the underlying InP. Detector contacts were made by Ti/Pt/Au mesa-roof metallisation and Ni/Ge/Au/Ni/Au back-wafer metallisation. The wafer was then thinned and cleaved to yield single WDM detector chips. No A.R. coating was applied to the input facet.

Array demultiplexers both with integrated detectors and without detectors were fabricated. A tunable laser and polarization controller was used with a lensed fiber to provide TE or TM input and the detector responses were measured on-chip at zero bias.

Results and discussion:

The response of one detector for incident TE and TM signals is shown in Figure 3. Within the measurement accuracy, the detector responses for TE and TM polarized light were identical; the spectral variation for TE and TM light and the absolute channel responses are indistinguishable.

The small difference in signal levels for the different channels (~ 1.4 dB in worst case) is ascribed to defects in the feed-guides leading to the detectors.

The wavelength channel spacings were found to be exactly 2 nm (± 0.06 nm r.m.s., on a spectral step of 0.1 nm), with no noticeable deviation across the 8-channel span; the 8-channel-span measured 14.0 nm, within the 0.1 nm accuracy of the scans.

The detectors recorded a passband FWHM of ~ 0.7 nm, in line with expectations, and identified a passband / channel spacing ratio of 35%. Cross-talk between channels was typically -16 dB, though somewhat higher for adjacent channels, at ~ -13 dB. Similar values were observed for demultiplexers that did not have photodetectors integrated, showing it to be optical in nature. The background value is higher than the best reported figures for raised-stripe array demultiplexers (< -25 dB, [6]), and is possibly associated with waveguide phase fluctuations arising from guide-width variations. This is consistent with typical demux excess losses of 6.5-7.5 dB, which is also higher than the value of ≤ 4.5 dB reported in that reference. (Some loss will also be associated with the planar/stripe-guide junctions.) Total on-chip loss of the detector shown was 9-10 dB, with an in-coupling loss of 3.9 dB (no AR-coating). Detector external responsivities were 0.05-0.065 A/W.

Conclusions:

We have demonstrated, for the first time, an integrated polarization-insensitive WDM detector. It comprised an arrayed waveguide demultiplexer employing raised-stripe 1.0Q InGaAsP guides and a p-i-n waveguide detector array. 8-channel WDM detection was demonstrated at precisely 2 nm-spaced channels without measurable polarization sensitivity. On-chip losses were 9.0-10.0 dB and channel cross-talk was -13 dB to -16 dB.

Acknowledgement: This work was supported in part by ARPA under grant MDA 972-92-H-0010.

- 1) J.B.D. Soole et al., *Appl. Phys. Lett.*, **6**, 1, 1992; J.B.D. Soole et al., *Electron. Lett.*, in press.
- 2) C. Cremer et al., *Phot. Tech. Lett.*, **4**, 108, 1992; C. Cremer et al., *E.C.I.O.* '93, 1993.
- 3) J.B.D. Soole et al., *Electron. Lett.*, **29**, 558, 1993.
- 4) M.R. Amersfoort et al., *E.C.O.C.* '93, paper THC12.13; M.R. Amersfoort et al., *Phot. Tech. Lett.*, **6**, 62, 1994.
- 5) M. Zimgibl et al., *I.P.R.C.* '94, paper FC4.
- 6) B.H. Verbeek et al., *O.F.C.* '94, paper PD13-1.

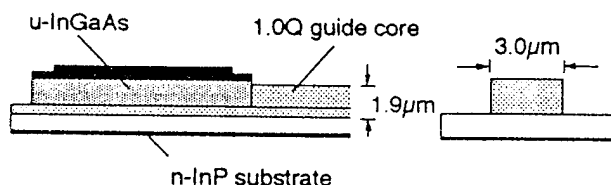


Fig. 1: Waveguide photodetector and raised-stripe guide.

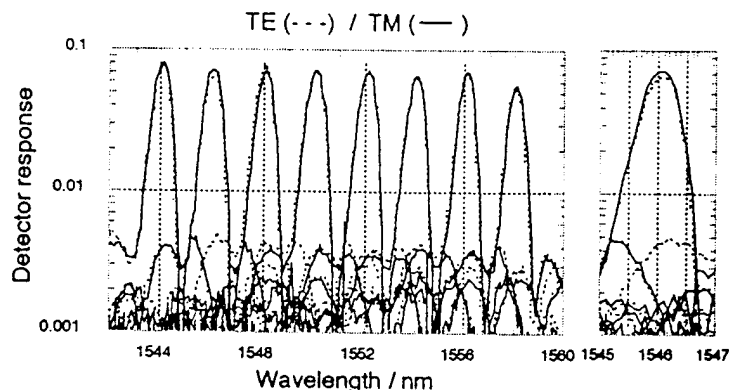


Fig. 3: TE response (dashed) and TM response (solid).
Also detail for one channel.

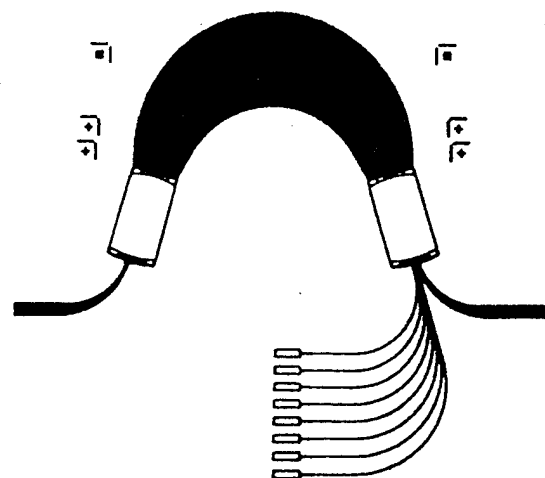


Fig. 2: Arrayed waveguide demux and detector array.
Die size is 3.7 mm x 4.0 mm

Packaged zero-loss polarization-independent four-channel Multi-Grating Filter

Jean-Pierre Weber

Ericsson Components AB, Fiber Optics Research Center,
S-164 81 Kista-Stockholm, Sweden
Tel.: +46-8-757-4513, Fax: +46-8-757-4764

Björn Stoltz, Marie Dasler

Ericsson Components AB, Opto and RF Power Products,
S-164 81 Kista-Stockholm, Sweden
Tel.: +46-8-757-4061

ABSTRACT

A four channel Multi-Grating Filter (at 1.55 microns) with polarization-independent channel positions and two integrated amplifiers has been fabricated in InGaAsP/InP. A packaged device has no fiber-to-fiber loss and worst case crosstalk below -18 dB.

Packaged zero-loss polarization-independent four-channel Multi-Grating Filter

Jean-Pierre Weber

Ericsson Components AB, Fiber Optics Research Center,
S-164 81 Kista, Sweden (+46-8-757-4513, Fax: +46-8-757-4764)

Björn Stoltz, Marie Dasler

Ericsson Components AB, Opto and RF Power Products,
S-164 81 Kista, Sweden (+46-8-757-4061)

One of the key component for the practical realization of Wavelength Division Multiplexing (WDM) transmission systems is a tunable optical filter or demultiplexer that allows the selection of the desired channel. Reported devices suitable for integration include filters based on active and passive DBR or DFB structures, (multiple) Mach-Zender interferometers and co-directional grating-assisted couplers (see references in [1]). Promising approaches include acousto-optic filters [2] and demultiplexers based on waveguide arrays [3, 4] or etched diffraction gratings [5, 6, 7]. We have taken yet a different approach with a device called a Multi-Grating Filter (MGF) [1, 8, 9]. The MGF acts as a demultiplexer by allowing only one channel (or eventually several channels) of a discrete set to be transmitted and blocking the other ones, but it acts as a filter in that the selection of the transmitted channel is controlled electrically.

To be useful in a real system, these filters and de-

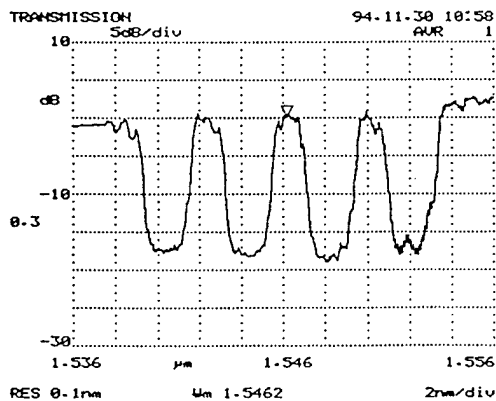


Figure 2 : Normalized transmission spectrum of a packaged MGF (#7) using the (unpolarized) spontaneous emission from an Erbium doped Fiber Amplifier (amplifier currents were 35 mA and 15 mA). [Add 1.6 nm to get the correct wavelengths]

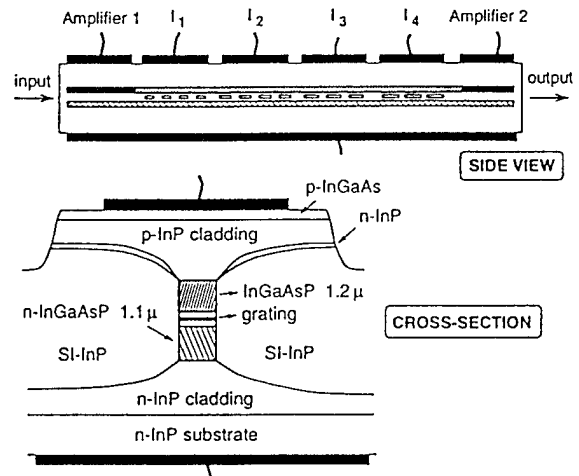


Figure 1: Structure of the four-channel polarization independent MGF with two integrated amplifier sections.

multiplexers have to be polarization insensitive. The MGF devices reported earlier [1, 8, 9] had about 4.5 nm difference between the channel wavelengths for the TE and the TM mode. In this paper, we present a Multi-Grating Filter with a new waveguide design which eliminates the TE/TM offset. Packaged devices with no fiber-to-fiber loss and worst case crosstalk below -18 dB have been fabricated.

As described previously in [1, 8, 9], the MGF uses several Bragg gratings in series in a waveguide (see Figure 1). Each grating center wavelength corresponds to one channel wavelength, so that all channels are blocked. A channel is selected by injecting current in the corresponding grating, which changes the center wavelength and allows the transmission of that channel. The center wavelength of a grating λ_c is given by $\lambda_c = 2n_{eff}\Lambda$, where Λ is the (physical) grating period and n_{eff} the effective index. The different gratings are fabricated with different Λ and the current injection changes n_{eff} through the plasma effect

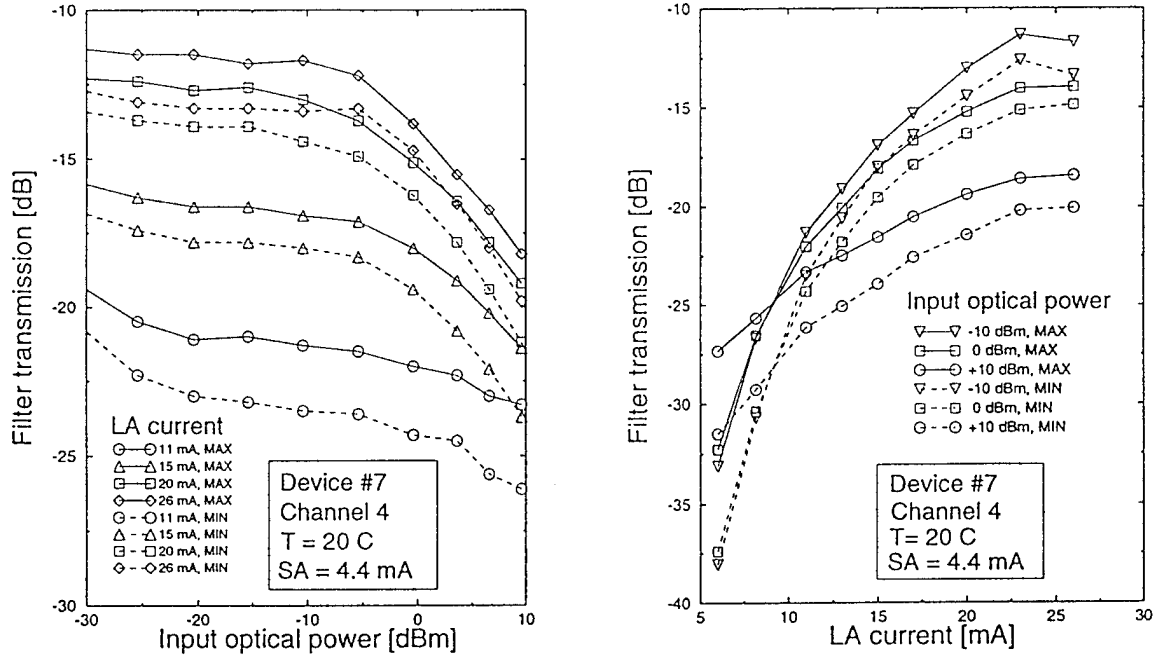


Figure 3: Packaged MGF #7: transmission of channel 4 (1552.4 nm) as a function of the LA current and input power in the fiber. SA is biased at transparency for that channel. MIN and MAX values for varying input polarizations are plotted.

of the injected carriers (see [10]). The TE and TM modes will have the same center wavelengths if they have the same n_{eff} .

This leads to a waveguide design with a nearly square cross-section. But there are several other constraints: single mode waveguide, large grating coupling coefficient κ (around 100 cm^{-1}), sufficient center wavelength shift with current injection (2 to 3 nm), waveguide as wide as possible ($> 0.5 \mu\text{m}$) to allow easy fabrication, reasonable tolerances. Using a vectorial finite element program to compute the effective indices, we arrived at the design shown in Figure 1. Using the refractive indices from [10] (at 300K, $1.555 \mu\text{m}$), calculations give $n_{eff} = 3.223$, $\kappa = 107 \text{ cm}^{-1}$, TE-TM difference = 0.05 nm. The most difficult dimension to control is the waveguide width. Calculations show that going from $0.7 \mu\text{m}$ to $0.8 \mu\text{m}$ increases the TE-TM offset to 0.25 nm and κ to 117 cm^{-1} , while the center wavelength shifts by 3.2 nm. Thus, the waveguide width should be controlled to better than $0.05 \mu\text{m}$, which is possible with electron-beam lithography and dry etching.

The devices (shown in Figure 1) are fabricated on a n-type InP substrate using low pressure MOVPE (Metal Organic Vapour Phase Epitaxy) for all the epitaxial growths. First the layers for the amplifier sections are grown: lower n-InP cladding, $0.6 \mu\text{m}$ n-InGaAsP ($1.1 \mu\text{m}$) waveguide layer, 50 nm n-InP, 50 nm n-InGaAsP ($1.4 \mu\text{m}$) grating layer, $0.1 \mu\text{m}$ n-InP,

$0.2 \mu\text{m}$ undoped InGaAsP ($1.58 \mu\text{m}$) active layer and top p-InP cladding. All n dopings are 10^{18} cm^{-3} and the p doping is $6 \times 10^{17} \text{ cm}^{-3}$. Then the grating regions are etched down to the grating layer and the gratings are formed by electron-beam lithography and etching in the grating layer. Then, 50 nm n-InP is regrown over the gratings, followed by a $0.5 \mu\text{m}$ undoped InGaAsP ($1.2 \mu\text{m}$) top waveguide layer and a top p-InP cladding layer. The $0.7 \mu\text{m}$ wide waveguide is then defined by electron-beam lithography and etched using reactive ion etching. After etching of the top p cladding between sections (for electrical isolation), semi-insulating (Fe doped) InP is selectively grown for current confinement. Finally, the top p contact layers are grown and metalization is done. Then the contact layers are removed between the sections. Each grating section is $400 \mu\text{m}$ long and the amplifiers are $450 \mu\text{m}$ (LA) and $250 \mu\text{m}$ long (SA) respectively. The waveguides terminate $20 \mu\text{m}$ from the anti-reflection coated facets (to reduce reflection). The filter was packaged the same way as in [9], with a Peltier element, thermistor and two lens couplers, except that we used normal fibers and no isolator.

Using polarization maintaining fiber tapers to couple light in and out of the device and the spontaneous emission from an EDFA as the light source, we measured less than 0.2 nm difference in center wavelength between TE and TM (before packaging). Some devices had no measurable difference ($< 0.1 \text{ nm}$). An

Open channel	Wavelength [nm]	Gain [dB]		On-off ratio [dB]	Crosstalk [dB] from channel				Transparency	
		max	min		1	2	3	4	SA [mA]	LA [mA]
1	1542.1	+1.7	-0.7	17.0	-	-22.4	-22.7	-25.0	5.2	9.8
2	1545.8	+2.8	-1.3	18.7	-18.5	-	-20.9	-23.0	4.9	9.2
3	1549.5	+2.5	-0.6	21.5	-18.1	-19.6	-	-24.2	4.6	8.6
4	1553.2	+3.5	+0.9	24.6	-20.3	-20.6	-24.6	-	4.4	8.2

Table 1: *Packaged MGF (device #7), input power = -9 dBm (tunable DBR laser), $T = 20^\circ\text{C}$ with currents of 26 mA in LA, 17 mA in SA (input side) and 20 mA for grating tuning. The transparency current of each amplifier for each channel wavelength is also given.*

unpolarized transmission spectrum of a packaged device is shown in Figure 2. The channel wavelengths are spaced by 3.7 nm (see Table 1). Temperature sensitivity of the channel positions is about 0.1 nm/K.

A tunable DBR laser was used to measure the transparency currents of the long (LA) and the short (SA) amplifier at each channel wavelength (Table 1). Then the gain and gain saturation of each amplifier was studied on a packaged device by measuring the transmission as a function of current and input optical power (with the other amplifier biased at transparency). Results are shown in Figure 3 for the long amplifier (LA) with channel 4. The solid and dashed curves are the maximum and minimum transmission (respectively) when the input polarization is varied. The other channels and SA give similar results: there seems to be an intrinsic 3 dB loss difference between the two polarizations and gain saturation appears above -5 dBm input optical power.

Fiber-to-fiber losses and worst case crosstalk (for any polarization combination) for a packaged MGF are shown in Table 1. Amplifier currents were 26 mA and 17 mA (grating tuning current = 20 mA), limited by the onset of lasing, and the input power was -9 dBm (SA side). For all channels, we have a fiber-to-fiber gain of about 1 dB, with about 3 dB polarization dependence. The crosstalk is between -18 dB and -25 dB in all cases. We estimated that the propagation loss on the chip (including the butt-joints) is only about 9 dB, while the amplifiers give about 16 dB and 8 dB gain respectively. This means that we have about 6.5 dB coupling loss per facet, which is high and may be due in part to the use of non-optimal lenses.

One remaining problem is the origin of the 3 dB polarization dependence of the losses. Part of this may be due to the design of the amplifier sections, which have a calculated confinement factor of 0.296 for TE and 0.231 for TM. And even in the gratings, free-carrier loss will be different for TE and TM due to different field distributions.

In conclusion, we have designed, fabricated and packaged a four-channel Multi-Grating Filter with

polarization independent channel wavelengths, no fiber-to-fiber loss and crosstalk below -18 dB.

This work was supported in part by the RACE MWTN (R2028) project.

References

- [1] J.-P. Weber, B. Stoltz, M. Dasler, and B. Kock, *Four-channel tunable optical notch filter using InGaAsP/InP reflection gratings*, IEEE Photon. Technol. Lett., vol. 6 (1), Jan 1994, pp 77-79.
- [2] R. Brinkmann, M. Dinand, I. Baumann, Ch. Harizi, W. Sohler, and H. Suche, *Acoustically tunable wavelength filter with gain*, IEEE Photon. Technol. Lett., vol. 6 (4), April 1994, pp 519-521.
- [3] M. Zirngibl, C.H. Joyner, L.W. Stulz, TH. Gaiffe and C. Dragone, *Polarization independent 8×8 waveguide grating multiplexer on InP*, Electron. Lett., vol. 29 (2), 21 Jan 1993, pp 201-202.
- [4] H. Bissessur, F. Gaborit, B. Martin, P. Pagnod-Rossiaux, J.-L. Peyre and M. Renaud, *16 channel phased array wavelength demultiplexer on InP with low polarization sensitivity*, Electron. Lett., vol. 30 (4), 17 Feb 1994, pp 336-337.
- [5] S.M. Ojha, G.H.B. Thompson, C.G. Cureton, C.B. Rogers, S.J. Clements, M. Asghari, and I.H. White, *Demonstration of low loss integrated InGaAsP/InP demultiplexer device with low polarization sensitivity*, Electron. Lett., vol. 29 (9), 29 April 1993, pp 805-807.
- [6] P.C. Clemens, G. Heise, R. März, H. Michel, A. Reichelt and H.W. Schneider, *8-channel optical demultiplexer realized as SiO₂/Si flat-field spectrograph*, IEEE Photon. Technol. Lett., vol. 6 (9), Sept 1994, pp 1109-1111.
- [7] C. Cremer, M. Schier, G. Baumeister, G. Ebbinghaus, H. Huber, W. Kunkel, J.G. Bauer, G. Kristen, J. Rieger, R. Schimpe, and R. Strzola, *WDM receiver chip with high responsivity*, Electron. Lett., vol. 30 (19), 15 Sept 1994, pp 1625-1626.
- [8] J.-P. Weber, B. Stoltz, M. Dasler, B. Kock, *New type of tunable optical filter using InGaAsP/InP gratings*, IPR'93 conf., March 22-24, 1993, Palm Springs, CA, paper PDP-5.
- [9] J.-P. Weber, B. Stoltz, M. Dasler and J. Walz, *Packaged tunable optical filter using InGaAsP/InP reflection gratings*, ECOC'94, Florence, Italy, September 25-29, 1994, paper Tu.P.7.
- [10] J.-P. Weber, *Optimization of the carrier-induced effective index change in InGaAsP/InP waveguides - Application to tunable Bragg filters*, IEEE J. Quantum Electron., vol. 30 (8), Aug 1994, pp 1801-1816.

Observation of Modulated Crosstalk in Multichannel Acoustooptic Switches

Janet Lehr Jackel and Jane E. Baran

Bellcore, NVC 3X359, 331 Newman Springs Rd., Red Bank, NJ 07701 (908)758-3147

David A. Smith and Rohini S. Chakravarthy

Case Western Reserve University

Daniel J. Fritz

United Technologies Research Center, 400 Main Street, East Hartford, CT 06108, (203) 727-7918

Abstract:

Crosstalk in acousto-optic switches is modulated at frequencies related to that of the acoustic waves driving the device. We present measurements of the modulation, a brief discussion of its causes and examples of its effect on system performance.

Observation of Modulated Crosstalk in Multichannel Acoustooptic Switches

Janet Lehr Jackel and Jane E. Baran

Bellcore, NVC3X359, 331 Newman Springs Road, Red Bank, NJ 07701 (908) 758-3147

David A. Smith and Rohini S. Chakravarthy

Department of Electrical Engineering, Case Western Reserve University, Cleveland OH 44106 (216)368-4073

Daniel J. Fritz

United Technologies Research Center, 400 Main Street, East Hartford, CT 06108 (203) 727-7918

Introduction: The interaction of channels in acoustooptic switches has not yet been fully characterized. In this paper we report observations of modulated crosstalk in these devices, and show that two different interaction mechanisms, both associated with the traveling-wave nature of the acousto-optic interaction, contribute to the observed modulation. This crosstalk can critically affect the performance of the switch in optical wavelength-routing crossconnects.

The acousto-optic switch, based on wavelength-dependent acousto-optic polarization conversion, is being investigated as a wavelength routing switch in WDM networks, primarily because it had been believed to offer simultaneous and independent switching of many closely-spaced wavelengths. Recent systems tests have shown that channel independence is only relative; nearby channels are, on the average, shifted towards each other, and switching efficiency is decreased.¹ We have shown recently that if the acousto-optic polarization converter is redesigned such that nearest neighbor channels are switched in separate sections of the device, these interactions are decreased, substantially restoring the independence of the channels.²

A related interaction between channels, which had been observed in the past, is the difference-frequency modulation of the signal when a second, nearby channels is selected.³ That is, when two acoustic frequencies, Ω_1 and Ω_2 , are used simultaneously, the optical output is found to be modulated at $\Delta\Omega = \Omega_1 - \Omega_2$. We will show here that modulation occurs at the acoustic driving frequencies, Ω_i , and at $2\Omega_i$, as well as at the sum and the previously observed difference frequencies, and that the dependence of modulation depth on the nature of the modulated light indicates that at least two processes are responsible. Because not all of the modulation can be eliminated, this effect may degrade the performance of acousto-optic switches when large numbers of channels are selected simultaneously.

Sources of sum and difference frequencies: There are at least two sources of sum and difference frequency

modulation in the AOTF, beating between frequency shifted components, and modulation at the acoustic frequencies of the polarization conversion efficiency.

(a) Frequency shifts: Beating between frequency-shifted optical components was commented on by Choy, et. al., in their paper describing observation of difference frequencies. When two acoustic waves are present, each produces polarization conversion at every wavelength. Conversion efficiency is determined both by the acoustic amplitude and by the extent to which it reconciles the TE-TM phase-mismatch. When phase matching is not accurate, conversion efficiency is low; thus the device is highly wavelength selective. Additionally, there is an accompanying optical frequency shift⁴ equal to the frequency of the acoustic wave. TE and TM components are shifted in opposite directions, and the direction of the shift depends on the relative direction of propagation of the optical and acoustic waves. Thus, when two channels are switched simultaneously, for light at any initial optical wavelength the polarization-converted light has two frequency-shifted components, one for each of the acoustic waves; these beat with each other to produce sum or difference frequencies, depending on the relative propagation direction of the two acoustic waves. We expect that:

- Such beating will be present whether or not the two acoustic waves overlap in the device.
- Beating should be seen only to the extent that the optical source is coherent.
- The size of the modulation will depend on the relative sizes of the two interfering waves, and therefore on both the conversion efficiency in a the desired channel and that due to sidelobes of other channels

In addition, if polarization isolation is imperfect, up and down conversion leads to modulation at the acoustic driving frequency and at twice that frequency, since the polarization-converted light can beat with unconverted, and therefore unshifted light or with light that has been shifted in the opposite direction. Thus we expect modulation at Ω and at 2Ω , even when only one

acoustic frequency is present, and at sum (or difference) frequencies where only difference (or sum) would be allowed in the perfect polarization case.

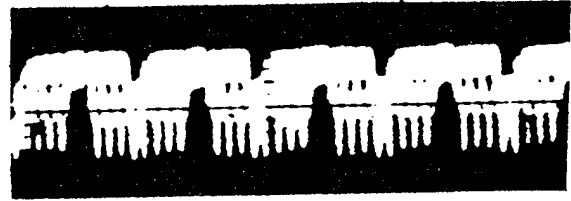
(b) **Modulation of conversion efficiency:** A second mechanism^{5,6} which generates sum or difference frequencies is the direct modulation of polarization conversion efficiency. Although the acousto-optic interaction leading to polarization conversion is linear, the dependence of the polarization conversion on acoustic amplitude is not. Indeed, the AOTF is really a directional coupler, a notoriously nonlinear device, with the acoustic wave providing the coupling between the TE and TM optical waves, and with a response proportional to $\sin(\kappa L)$, where κ is the coupling strength and L the length of the device. With two acoustic waves present in the device simultaneously, the coupling coefficient is modulated at their difference or sum frequency, depending of relative propagation direction for the acoustic waves, leading to modulation of the polarization conversion efficiency at those frequencies. When the polarization conversion is overdriven (i.e., $\kappa L > \pi/2$) higher harmonics of the difference (or sum) will also be generated. We can conclude that:

- Sum and difference frequency modulation due to nonlinearity is proportional to the overlap of the acoustic waves.
- Modulation does not require a coherent light source. The polarization conversion efficiency is being modulated, and the nature of the optical signal is irrelevant.
- The size of the modulation is not related to the sidelobe intensity.

Device Configuration and Measurements: We have made all measurements using a passband-flattened⁷ apodized⁸ AOTF, with an acoustic absorber dividing the interaction region in half and two IDTs, which allow each half of the device to be addressed independently. If the absorber is complete, we call this an apodized device, and if the absorber allows some of the acoustic wave to pass through it, this is a passband-flattened AOTF. Thus we can look at copropagating acoustic waves with total overlap, and counterpropagating acoustic waves with no overlap or with small overlap, but not non-overlapping acoustic waves propagating in the same direction.

In order to characterize the sum and difference frequency modulation, input light, either the locally "white light" of an EDFA, a narrow line laser, or the laser output amplified through the EDFA, is polarized, passes through the AOTF, and then through a second polarizer. The output is split, with half going to an

a.



b.

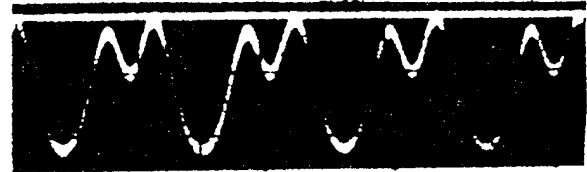


Fig. 1 Difference frequency modulation of bar state output (a) at 500 kHz, where input is a laser modulated at 300 kHz and (b) at 200 kHz, with unmodulated input; with wavelength interaction overdriven, higher harmonics are produced. Bar state average rejection is -16dB.

optical spectrum analyzer and half to an optical RF spectrum analyzer. Thus we can monitor both the optical and the RF spectrum simultaneously. In an alternative measurement, part of the optical output is detected and displayed on an oscilloscope (Fig. 1).

Results: For all measured device configurations both sum and difference frequency modulations were observed, and in addition, the optical output was modulated at both the acoustic driving frequency, Ω and at 2Ω . Fig. 2 shows a typical RF spectrum. In some, but not all cases we also observed modulation at $2(\Omega_1 - \Omega_2)$ and higher harmonics. Relative modulation depths depend on the device configuration, the nature of the optical signal, and the frequency separation of the acoustic waves. The data indicate that both proposed mechanisms are contributing. With a laser input, we see modulation, **independent of acoustic wave overlap**, as predicted from beating between frequency shifted components. As expected, the depth of modulation is correlated with sidelobe height. The modulation depth at Ω and 2Ω could be reduced almost to zero by improving polarization isolation, also in agreement with the above arguments.

However, with the EDFA alone used as input we expect no contribution from this mechanism, and indeed the observed modulation is strongly dependent on both acoustic wave overlap and relative acoustic wave propagation direction. Strong modulation is seen only for the case where both acoustic waves propagate in the same direction in the same section of the device, and only the difference frequency is strong.

The worst-case difference frequency modulation is about -10 dB. Modulation due to up and down conversion can be minimized by increasing peak

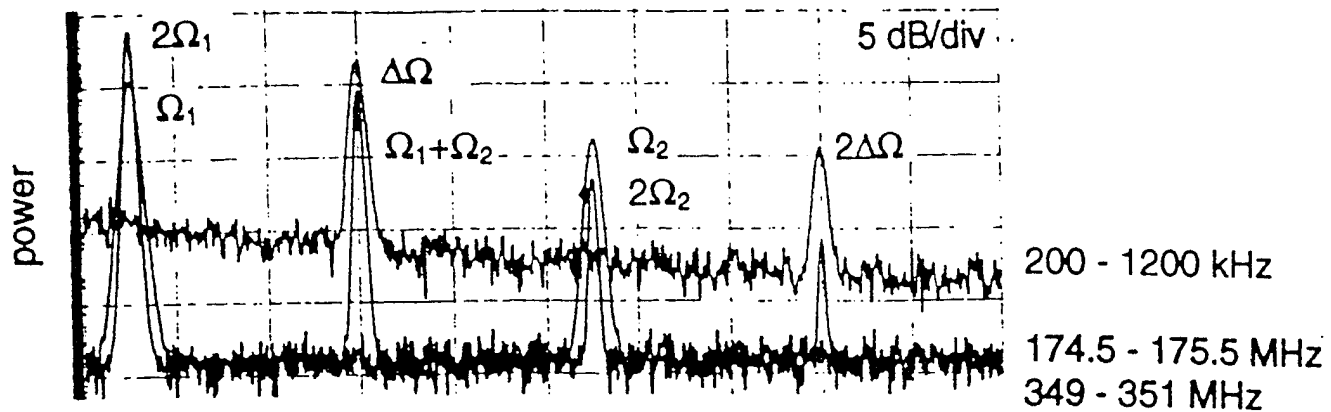


Fig. 2 RF spectra covering three frequency ranges, superimposed to show simultaneous generation of sum, difference, acoustic drive, and twice acoustic drive frequencies. Because the switch is "overdriven" we also see twice the difference frequency.

conversion efficiency, flattening the passband, and decreasing sidelobes; modulation of the conversion efficiency appears to be intrinsic to the device, but can be limited by increasing the channel spacing to channel width ratio, and by lengthening the device.

Consequences: The presence of modulation at these frequencies has little effect on the signal intended to be passed through the filter. Even the worst modulation of about -10 dB results in only a 10% variation in the intensity of the signal. However, the effect on *crosstalk* is more severe. A modulation of 10% of the signal implies that the worse case crosstalk will be at least -10 dB. While switch dilation can reduce this to -20 dB, this level of crosstalk is great enough to limit the usefulness of this switch for certain applications. For example, we have observed a power penalty for high bit rate signals when four close-spaced channels are switched simultaneously. Fig. 4 shows BER

measurements made at 2.48 Gb/s with 1,3, and 4 channels selected. We believe that the increase in BER is at least partly attributable to time-dependent crosstalk.

Acknowledgments: We thank Evan Goldstein for valuable discussion of the systems level consequences of the observed modulation. This work was supported in part by the US Advanced Research Projects Agency (ARPA).

References

1. G.-K. Chang and M. Z. Iqbal, personal communication.
2. J. L. Jackel, et. al., "Multichannel operation of AOTF switches with minimal channel-to-channel interaction," OFC'95; to be published in *Photon. Technol. Lett.*, April 1995.
3. M. Choy, et. al., "Observation of Coherent Interchannel Interference in the Multiwavelength Operation of an Acoustooptic Filter," *IEEE Photon. Technol. Lett.*, 1, 171-172 (1989).
4. F. Heismann and R. Ulrich, "Integrated-Optical Single-Sideband Modulator and Phase Shifter," *IEEE JQE*, QE-18, 767-771 (1982).
5. G. H. Song, et. al., "Time-Dependent Model of an Acousto-Optic Tunable Filter for Multiple-Channel Operation," IPR'95
6. D. A. Smith, R. S. Chakravarthy, L. Trollo, and A. d'Alessandro, "Passband Collisions and Multi-Channel Crosstalk in Acousto-Optic Filters and Switches," submitted to ECIO'95.
7. J. L. Jackel, et. al., "A passband-flattened acousto-optic filter," to be published in *Photon. Technol. Lett.*, March 1995.
8. D. A. Smith and J. J. Johnson, "Sidelobe suppression in an acousto-optic filter with a raised-cosine interaction strength," *Appl. Phys. Lett.* 61, 1025-1027 (1990).

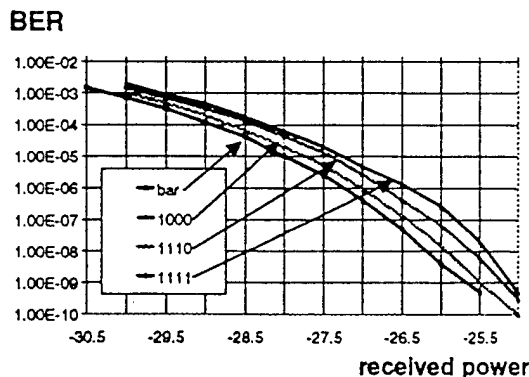


Fig. 3 BER measurements made at 2.48 Gb/s, comparing behavior of acoustooptic switch with one (1000), three (1110), or four (1111) channels switched.

Acoustic Pulse Measurements of Acousto-Optic Tunable Filter Properties

L. B. Aronson, G. Rankin, T. R. Ranganath, D. W. Dolfi

Hewlett Packard Laboratories, 3500 Deer Creek Road Bldg 26M,
Palo Alto, CA. 94303-0867. Tel. 1-415-857-4293

Abstract

Spatially resolved measurement of waveguide birefringence and acoustic interaction strength in Acousto-Optic Tunable Filters is demonstrated using short acoustic pulses.

Acoustic Pulse Measurements of Acousto-Optic Tunable Filter Properties

L. B. Aronson, G. Rankin, T. R. Ranganath, D. W. Dolfi

Hewlett Packard Laboratories, 3500 Deer Creek Road Bldg 26M,
Palo Alto, CA. 94303-0867. Tel. 1-415-857-4293

Summary

There is a great deal of interest in Acousto-Optic Tunable Filters (AOTFs) for wavelength division multiplexing applications because of their fast tuning speeds, wide tuning ranges and the ability to switch multiple wavelengths simultaneously.¹ One practical limitation of these devices has been sidelobe levels which are often much larger than expected by theory. This is the case both in uniform devices as well as those where apodization techniques to reduce sidelobes are employed. Trutna *et al.*² explained these anomalous sidelobes as being the result of longitudinal birefringence variations in the AOTF waveguides. These variations could be due to numerous sources such as waveguide width and doping variations, thermal gradients, substrate birefringence variations and stress induced birefringence variations. While it was useful to know the general source of high sidelobes, the shape of the filter function does not directly yield the location of the problem, or help with finding a solution.

Here we report a new measurement technique which gives a spatially resolved map of the birefringence of the waveguide as well as the strength of the SAW wave and the acousto-optic interaction. Additionally, we give two measurement examples which demonstrate the usefulness of the technique in device development. The basic experimental setup is shown in Figure 1. Polarized light is launched into the AOTF and the output passes through a crossed polarizer and onto a detector. The acoustic transducer of the AOTF is driven with a short pulse of RF. Because the fractional bandwidth of a typical AOTF transducer is 10% or more, it is possible to generate acoustic pulses as short as 0.1 μ s. Based on the SAW velocity of 3750 m/s, this corresponds to an acoustic pulse length of 0.375 mm which is much shorter than the device. We can then record the output as a function of time as the pulse travels down the device length. The resulting output is a spatial map of the acousto-optic interaction strength along the length of the device for the RF frequency used.

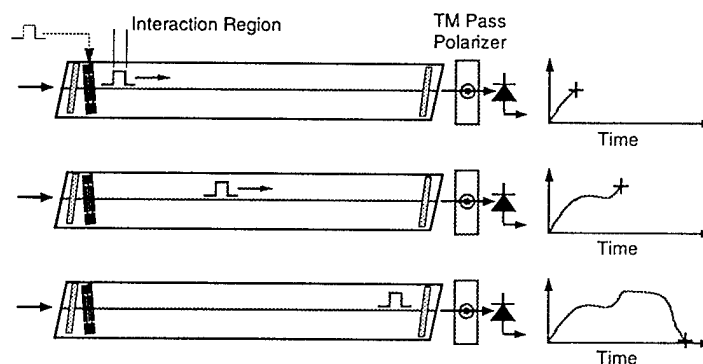


Fig 1. Basic setup for pulsed acoustic measurements

Variations in the acousto-optic interaction strength can be due to two causes:

- 1) Variations in the acousto-optic coupling constant κ .
- 2) Variations in the phase mismatch parameter, $\Delta\beta$ (birefringence).

We have identified two measurement modes based on short or long pulses which can be used to sort out these two effects. First, let us examine the sensitivity to width and temperature variations as a function of pulse length. Assuming that the coupling strength and phase mismatch are uniform within the pulse, the converted output is given by:

$$P_{out} = \frac{(\kappa L)^2}{(\kappa L)^2 + \left(\frac{\Delta\beta L}{2}\right)^2} \sin^2 \left(\sqrt{(\kappa L)^2 + \left(\frac{\Delta\beta L}{2}\right)^2} \right) \quad (1)$$

where $L = v_a \tau$ is the pulse length, κ is the coupling constant and $\Delta\beta$ is the phase mismatch:

$$\Delta\beta = \frac{2\pi\Delta n}{\lambda} - \frac{2\pi f_a}{v_a} \quad (2)$$

For the typical short pulse case where $\kappa L \ll \pi/2$, the FWHM of equation (1) in terms of $\Delta\beta$ is:

$$\Delta\beta_{FWHM} = \frac{5.6}{L} = \frac{5.6}{v_a \tau} \quad (\kappa L \ll 1) \quad (3)$$

Using measured dependencies of birefringence on waveguide width and temperature, the required waveguide width and temperature variations to reduce the output by half are then:

$$\delta w_{1/2} \approx \frac{1.15 \mu m}{\tau(\mu s)} \quad \delta T_{1/2} \approx \frac{5.35^\circ C}{\tau(\mu s)} \quad (4)$$

If a very short pulse is used (say 0.1 μs), the output is found to be very insensitive to realistic birefringence variations. For example, the waveguide width would have to vary by 11.5 μm or the temperature by 53°C to reduce the output by half. Given that $\Delta\beta$ is effectively 0 in the short pulse regime, we find that the output becomes:

$$P_{out}(\text{short pulse}) \approx \sin^2(\kappa L) \approx (\kappa L)^2 \sim P_a \quad (5)$$

Thus the output becomes a map of the square of the coupling constant only which, if we assume a uniform acousto-optic coefficient, is proportional to the acoustic power. An example of this measurement is shown in Figure 2. This data shows that there is not undo attenuation or walk-off of the acoustic wave.

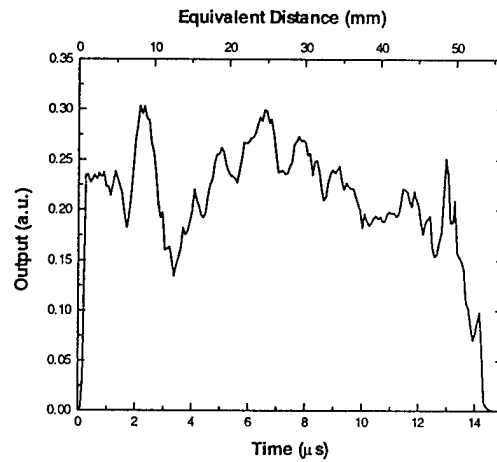


Fig 2. Short pulse measurement results showing acoustic power uniformity

In the long pulse regime (e.g. 2 μs) there is reduced spatial resolution, but the output is sensitive to phase mismatch as well as the coupling constant. By taking a series of measurements at

different acoustic frequencies, we can build up a contour map as shown in Figure 3. In this plot, we have made time (which is equivalent to position along the waveguide) the x axis. The y-axis is the acoustic frequency. In an ideal device with an on axis transducer, the plot should show a uniform horizontal ridge centered on the phasematching frequency. Birefringence variations will be seen as curvature of that ridge, and acoustic power variations will be seen as variations of the ridge height. The device measured in Figure 3 is shown on the right. It is a standard single section AOTF with the transducer offset laterally and rotated such that the acoustic beamwalks on and then off the waveguide with the aim of providing a simple form of amplitude apodization. In the resulting contour plot, we can see both the amplitude apodization as well as a small amount of curvature indicating a birefringence nonuniformity. The righthand axis of the plot calibrated the birefringence offset in terms of equivalent waveguide width variations.

We have already used this technique to solve a packaging problem where stress induced birefringence varied with time. In that case, the shape of the filter function varied as the temperature of the package was cycled, with a very long recovery time. Using these techniques, it was possible to identify where the chip was epoxied to the package and where it was free to be stretched. The ability to measure the acoustic power as a function of distance should also be useful in designing amplitude apodization schemes. Previously, the only way to evaluate these ideas was to use a SAW probe, which requires a highly specialized measurement setup.

In summary, we have described a new measurement technique for AOTFs which provides spatially resolved data on the birefringence and acoustic power non-uniformities in the waveguide. This technique is simple to implement and requires no special equipment other than a pulsed RF source. In addition to various AOTF applications, this technique may be valuable for evaluating waveguide or package stress problems in other LiNbO_3 integrated optical devices.

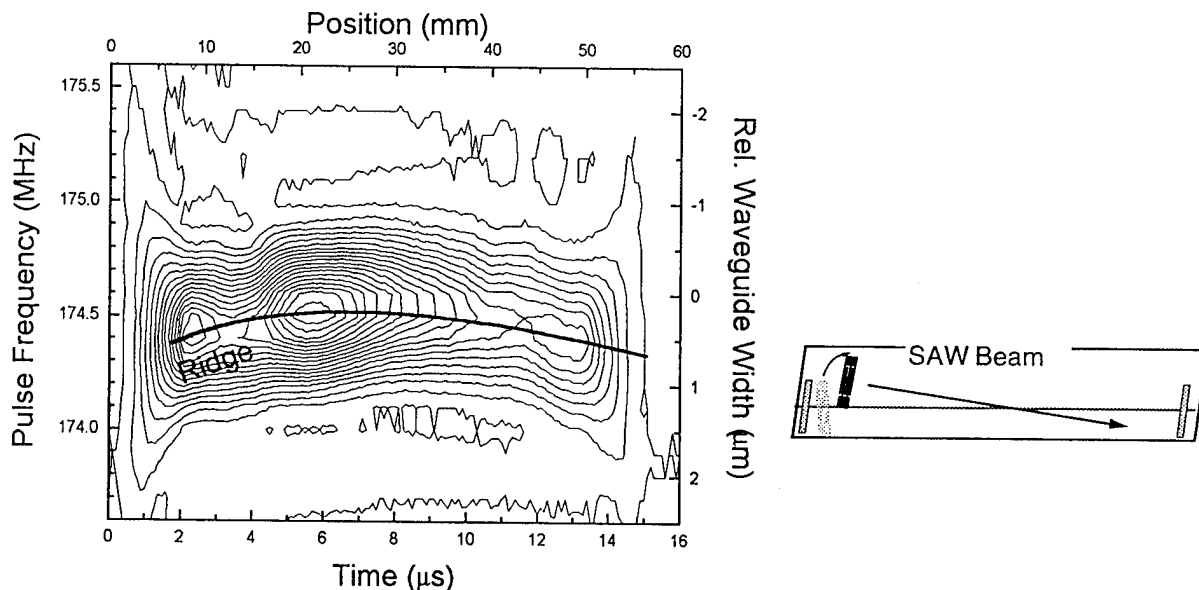


Fig 3. Long pulse measurements at various frequencies showing waveguide uniformity and amplitude apodization in an AOTF with an offset rotated transducer (right).

1. D. A. Smith, J. E. Baran, J. J. Johnson and K. W. Cheung, *IEEE J. Sel. Comm.* **8**, 1151 (1990).
2. W. R. Trutna, Jr., D. W. Dolfi, and C. A. Flory, *Opt. Lett.* **18**, 28 (1993).

Basic Design Rule of 1.3- μ m InP-Based Strained MQW Lasers for High Temperature Operation

S. Seki, H. Oohashi, H. Sugiura, T. Hirono, and K. Yokoyama

NTT Opto-electronics Laboratories

3-1 Morinosato Wakamiya, Atsugi, Kanagawa, 243-01 Japan

(Tel: 81-462-40-3173, Fax: 81-462-40-2859)

Abstract

Basic design rule for highly-efficient operation of 1.3- μ m InP-based strained MQW lasers at elevated temperatures is derived on the basis of a self-consistent numerical approach. The validity of the design rule is experimentally demonstrated by the excellent performance ($\eta=0.55$ W/A and $P_{\max} > 35$ mW at 363 K) of fabricated lasers.

Basic Design Rule of 1.3- μm InP-Based Strained MQW Lasers for High Temperature Operation

S. Seki, H. Oohashi, H. Sugiura, T. Hirono, and K. Yokoyama

NTT Opto-electronics Laboratories

3-1 Morinosato Wakamiya, Atsugi, Kanagawa, 243-01 Japan

(Tel: 81-462-40-3173, Fax: 81-462-40-2859)

InP-based strained-layer (SL) multiple-quantum-well (MQW) lasers operating at a wavelength of 1.3 μm are of much interest due to their applications to fiber-in-the-loop (FITL) and fiber-to-the-home (FTTH) systems [1], [2]. For these applications, high efficiency and high output power are required as well as low threshold current over a wide range of operation temperatures. In this paper, we derive a basic design rule for highly-efficient operation of InP-based SL-MQW lasers at elevated temperatures on the basis of a self-consistent numerical approach.

The band offset in InP-based SL-MQWs is significantly changed under high-injection conditions [3], [4]. To take into account the changes in band offset due to electrostatic band-profile deformation, the band structures were obtained by self-consistently solving the Poisson equation, the scalar effective-mass equation for the conduction band, and the multi-band effective-mass equation for the valence band. To properly include the strain-dependent coupling, a 6×6 Luttinger-Kohn Hamiltonian was used for the valence-band Hamiltonian. The conduction-band Hamiltonian was assumed to be parabolic in \mathbf{k} -space.

In this study, we focus on two design parameters: (i) the ratio of radiative current component, $J_{\text{rad}}^{1-1}/J_{\text{rad}}^{\text{total}}$, and (ii) the threshold carrier density. Here, J_{rad}^{1-1} is the radiative current component resulting from the transition between the ground states in the conduction and valence bands, and $J_{\text{rad}}^{\text{total}}$ is the total radiative current density. Hence, $J_{\text{rad}}^{1-1}/J_{\text{rad}}^{\text{total}}$ is a good measure of carrier confinement in the QWs.

We analyzed an MQW structure with compressively-strained $\text{InAs}_y\text{P}_{1-y}$ ($y = 0.52$) [5] as the active region. The amount of strain and the QW thickness were adjusted to be 1.5% and 6 nm [6]. The MQW stack, which incorporates three QWs with barriers of 10-nm InGaAsP, is sandwiched between 50-nm InGaAsP separate confinement heterostructure (SCH) layers. To clarify the influence of carrier spillover, three different compositions of InGaAsP were used for the SCH layers: $\lambda_g = 1.1, 1.05$ and $1.0 \mu\text{m}$ (referred to hereafter as Q1.1, Q1.05, and Q1.0, respectively). The composition of barrier layers is the same as that of SCH material in each case.

The physical meaning of $J_{\text{rad}}^{1-1}/J_{\text{rad}}^{\text{total}}$ is more clearly indicated in Fig. 1, which shows the spontaneous emission spectra for SL-MQWs with Q1.1 barrier and SCH layers when the mode gain ΓG_p is 30 cm^{-1} . Here, Γ is the optical confinement factor and G_p is the peak value of optical gain. The shaded area corresponds to the radiative current component J_{rad}^{1-1} . It is noted that the peak corresponding to the band-gap energy of the

barrier and SCH material (i.e., about 1.1 eV) is notably enhanced, which agrees well with experimentally observed spectra changes [7]. These results clearly indicate that it is necessary to take into account electrostatic band-profile deformation to accurately determine the design parameter $J_{\text{rad}}^{1-1}/J_{\text{rad}}^{\text{total}}$ at elevated temperatures.

Figure 2 shows the variations in $J_{\text{rad}}^{1-1}/J_{\text{rad}}^{\text{total}}$ relative to mode gain, using the composition of the barrier and SCH material as a parameter. The results for two different temperatures are compared. Note that the band-gap energy of the barrier and SCH material has a pronounced influence on $J_{\text{rad}}^{1-1}/J_{\text{rad}}^{\text{total}}$ at elevated temperatures. These results suggest that the efficiency of lasers at elevated temperatures is significantly enhanced by using the barrier and SCH materials with larger band-gap energy. However, increasing band-gap energy of these materials could significantly reduce the optical confinement factor, leading to an increase in threshold carrier density (N_{th}). Hence, it is necessary to make a trade-off between $J_{\text{rad}}^{1-1}/J_{\text{rad}}^{\text{total}}$ and N_{th} . The variations in N_{th} with changes in mode gain are plotted in Fig. 3, using the composition of barrier and SCH layers as a parameter. Over a wide range of mode gain ($3\text{--}10\text{ cm}^{-1}/\text{well}$), Q1.05 gives the lowest N_{th} regardless of temperature, while Q1.0 increases N_{th} . These results indicate that, to maximize device performance for a required mode gain at elevated temperatures, SL-MQW structures should be designed so as to maximize $J_{\text{rad}}^{1-1}/J_{\text{rad}}^{\text{total}}$ without paying much penalty in N_{th} .

Applying the derived design rule, we fabricated SL-MQW Fabry-Perot buried heterostructure (BH) lasers. The SL-MQW stack, which consists of six $\text{InAs}_y\text{P}_{1-y}$ ($y = 0.52$) QWs with 1.5% compression, was grown by chemical beam epitaxy [8]. In accordance with the results shown in Figs. 2 and 3, we chose Q1.05 for the barrier and SCH layers. Figure 4 shows the CW light-current characteristics of SL-MQW BH lasers. The laser cavity is $300\text{-}\mu\text{m}$ long with a high reflection coating ($R_r = 96\%$) on the rear facet. The threshold current is 6.5 mA at 303 K and the characteristic temperature (T_0) of threshold current is 56 K in the temperature range of 303–373 K. Note that very high efficiency of 0.55 W/A is obtained at 363 K. This makes it possible to reduce the drive current required for high power operation at elevated temperatures. At 363 K, the output power is 30 mW at drive currents as low as 100 mA. This output power at 363 K is more than one and half times as large as that when Q1.1 or Q1.0 was used for the barrier and SCH layers under the same current condition. The maximum possible power at 363 K exceeds 35 mW by further increase in drive current. These results clearly indicate the validity of the derived design rule.

In summary, we have derived a basic design rule of $1.3\text{-}\mu\text{m}$ InP-based SL-MQW lasers for high temperature operation. The design rule, which was obtained on the basis of a self-consistent numerical approach including the Poisson equation and the effective-mass equations for the conduction and valence bands, is to maximize the ratio of $J_{\text{rad}}^{1-1}/J_{\text{rad}}^{\text{total}}$ for a required mode gain without paying much penalty in N_{th} . Following this rule, high-efficiency (0.55 W/A at 363 K) and high-power (over 35 mW at 363 K) InP-based SL-MQW BH lasers have been fabricated.

References

- [1] P. J. A. Thijs et al., IEEE J. Lightwave Technol. LT-12, 28 (1994).
- [2] C. E. Zah et al., IEEE J. Quantum. Electron. QE-30, 511 (1994).
- [3] G. Fuchs et al., Phys. Rev. B, 48, 15175 (1993).
- [4] S. Seki et al., to be published in IEEE Photon. Technol. Lett.
- [5] M. Yamamoto et al., IEEE J. Quantum. Electron. QE-30, 554 (1994).
- [6] S. Seki et al., J. Appl. Phys. 76, 3250 (1994).
- [7] H. Temkin et al., Digest of IPRM'94, Santa Barbara, MA2 (1994).
- [8] H. Sugiura et al., to be published in J. Cryst. Growth.

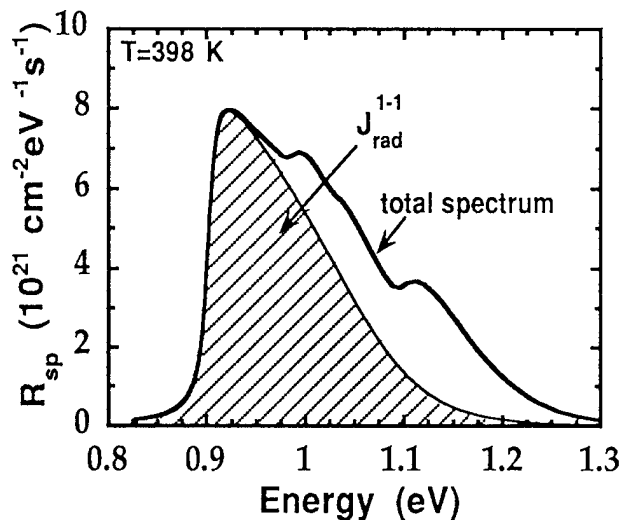


Fig. 1 Calculated spontaneous emission spectra of compressively-strained InAsP MQW lasers.

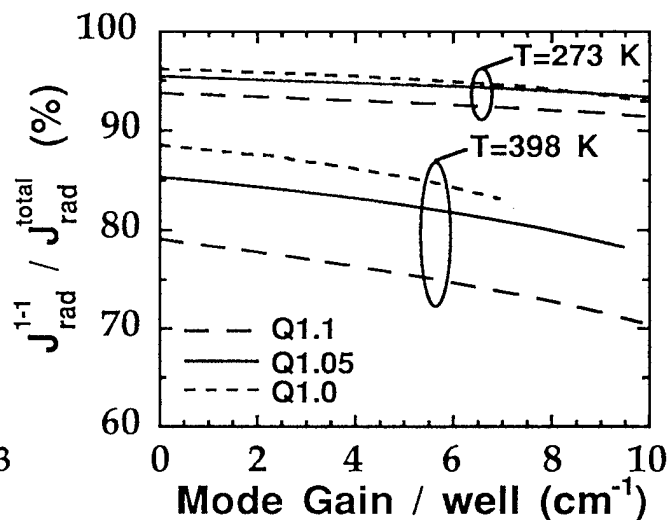


Fig. 2 Current component ratio plotted as a function of mode gain using the composition of the barrier and SCH material as a parameter.

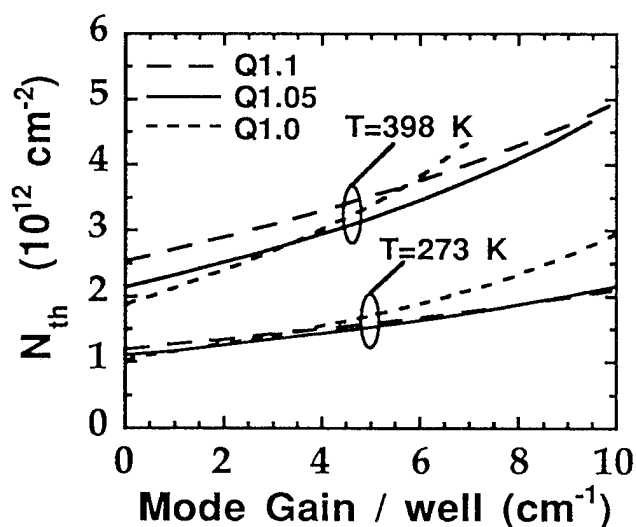


Fig. 3 Threshold carrier density plotted as a function of mode gain using the composition of the barrier and SCH material as a parameter.

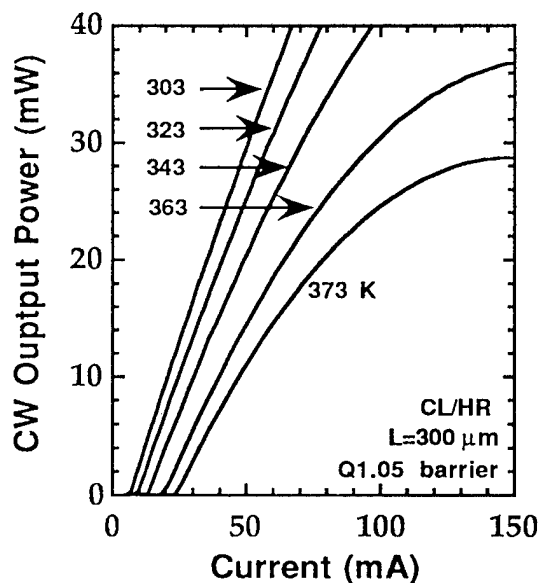


Fig. 4 CW light-current characteristics of a compressively-strained InAsP MQW laser.

The Application of the Alternating Directional Vector Beam Propagation Method to Semiconductor Rib Waveguide Y-Junctions

Jun Yu

Advanced Technology Laboratory
Bell Northern Research Ltd.
P.O. Box 3511, Station C
Ottawa, Ont. K1Y 4H7

David Yevick

Department of Electrical Engineering
Kingston, Ontario K7L 3N6, Canada

Witold Bardyszewski

Institute of Theoretical Physics, Warsaw University
Hoza 69, Warsaw, Poland

Abstract

We outline and examine numerically an efficient full vectorial beam propagation algorithm based on the alternating direction implicit (ADI) finite difference method.

Introduction: While relaxation procedures for determining the vector modes of waveguides can be immediately converted into imaginary distance propagation methods,[1] full vector beam propagation techniques in real space are intrinsically unstable[2]. Further as alternating directional methods can only be applied to a particularly divergent form of the vector wave equation (although they are easily adapted to the quasivectorial approximation)[3], the computational effort required in current propagation programs is often excessive. Direct finite difference methods, while rapid, are only conditionally stable, and thus may require small step sizes for certain refractive index profiles[4].

In this paper, we consider a novel alternating directional implicit (ADI) procedure, first proposed in [5], for the full vector wave equation. This method is shown to be rapid and simple to implement numerically. We then apply the procedure to the test case of a longitudinally varying semiconductor rib waveguide Y-junction, obtaining results which yield physical insight regarding the mutual coupling between the two polarizations.

Numerical Method: We consider the vector wave equation, which can be written in the compact form

$$-\frac{\partial^2}{\partial z^2} E_\alpha = k_0^2 n_0^2 E_\alpha + k_0^2 (n^2 - n_0^2) E_\alpha + \sum_{\beta=x,y} \left[\frac{\partial}{\partial \alpha} \left(\frac{1}{n^2} \frac{\partial}{\partial \beta} (n^2 E_\beta) \right) + (\delta_{\alpha\beta} - 1) \left(\frac{\partial^2 E_\beta}{\partial \alpha \partial \beta} - \frac{\partial^2 E_\alpha}{\partial \beta^2} \right) \right]$$

$$\equiv k_0^2 n_0^2 \sum_{\beta} (\delta_{\alpha\beta} + H_{\alpha\beta}) E_\beta \quad (1)$$

with $\alpha, \beta \in \{x, y\}$.

If the off-diagonal terms in the operator H are expressed as $\frac{1}{k_0^2 n_0^2} \left(\frac{\partial \log n^2}{\partial \beta} \frac{\partial}{\partial \alpha} + \frac{\partial^2 \log n^2}{\partial \alpha \partial \beta} \right)$,

H can be immediately separated into a term containing only x derivative and a second term containing y derivative. While such a procedure immediately enables the construction of a ADI method, the presence of second-order cross-derivatives of the refractive index gives rise to a high degree of instability in the resulting propagation algorithms. Accordingly, we instead seek a ADI procedure for the unmodified Eq.(1).

Introducing the paraxial approximation $E_\perp(x, y, z) = \Psi_\perp(x, y, z) e^{-jn_0 k_0 z}$ the formal solution to Eq.(1) can be written as

$$\begin{bmatrix} \Psi_x(z + \Delta z) \\ \Psi_y(z + \Delta z) \end{bmatrix} = e^{\frac{\Delta z}{2jk_0 n_0} \begin{bmatrix} a_{11} & 0 \\ 0 & a_{22} \end{bmatrix}} e^{\frac{\Delta z}{2jk_0 n_0} \begin{bmatrix} b_{11} & 0 \\ 0 & b_{22} \end{bmatrix}} e^{\frac{\Delta z}{2jk_0 n_0} \begin{bmatrix} 0 & M_{xy} \\ M_{yx} & 0 \end{bmatrix}} \cdot \begin{bmatrix} \Psi_x(z) \\ \Psi_y(z) \end{bmatrix} \quad (2)$$

in which $a_{11} = \frac{\partial}{\partial x} \frac{1}{n^2} \frac{\partial}{\partial x} n^2 + 0.5 k_0^2 (n^2 - n_0^2)$, $a_{22} = \frac{\partial^2}{\partial x^2} + 0.5 k_0^2 (n^2 - n_0^2)$, $b_{11} = \frac{\partial^2}{\partial y^2} + 0.5 k_0^2 (n^2 - n_0^2)$,

$b_{22} = \frac{\partial}{\partial y} \frac{1}{n^2} \frac{\partial}{\partial y} n^2 + 0.5 k_0^2 (n^2 - n_0^2)$, $M_{xy} = \frac{\partial}{\partial x} \frac{1}{n^2} \frac{\partial}{\partial y} n^2 - \frac{\partial^2}{\partial x \partial y}$, and $M_{yx} = \frac{\partial}{\partial y} \frac{1}{n^2} \frac{\partial}{\partial x} n^2 - \frac{\partial^2}{\partial y \partial x}$.

While the two leftmost exponential operators may be evaluated using standard splitting procedures, a coordinate transformation is required to apply the ADI method to the third operator[6]. After discretization

on a two-dimensional uniform grid with $N_x \times N_y$ points yields

$$M_{xy} \Psi_y^{i,j} = \frac{1}{4\Delta x \Delta y} \begin{bmatrix} a_1 & a_2 & a_3 & a_4 \end{bmatrix} \begin{bmatrix} \Psi_y^{i+1,j+1} & \Psi_y^{i+1,j-1} & \Psi_y^{i-1,j+1} & \Psi_y^{i-1,j-1} \end{bmatrix}^T$$

with $a_1=(n_{i+1,j+1}^2/n_{i+1,j}^2)-1$, $a_2=(-n_{i+1,j-1}^2/n_{i+1,j}^2)+1$, $a_3=(-n_{i-1,j+1}^2/n_{i-1,j}^2)+1$, and $a_4=(n_{i-1,j-1}^2/n_{i-1,j}^2)-1$ and

$$M_{yx} \Psi_x^{i,j} = \frac{1}{4\Delta x \Delta y} \begin{bmatrix} b_1 & b_2 & b_3 & b_4 \end{bmatrix} \begin{bmatrix} \Psi_x^{i+1,j+1} & \Psi_x^{i-1,j+1} & \Psi_x^{i+1,j-1} & \Psi_x^{i-1,j-1} \end{bmatrix}^T$$

in which $b_1=(n_{i+1,j+1}^2/n_{i,j+1}^2)-1$, $b_2=(-n_{i-1,j+1}^2/n_{i,j+1}^2)+1$, $b_3=(-n_{i+1,j-1}^2/n_{i,j-1}^2)+1$, and $b_4=(n_{i-1,j-1}^2/n_{i,j-1}^2)-1$. The superscript T denotes transpose.

In practice, we first apply a one-dimensional finite difference method to each of the downward sloping and then to the upward sloping diagonals of the two-dimensional grid of electric field values shown in the following schematic diagram.

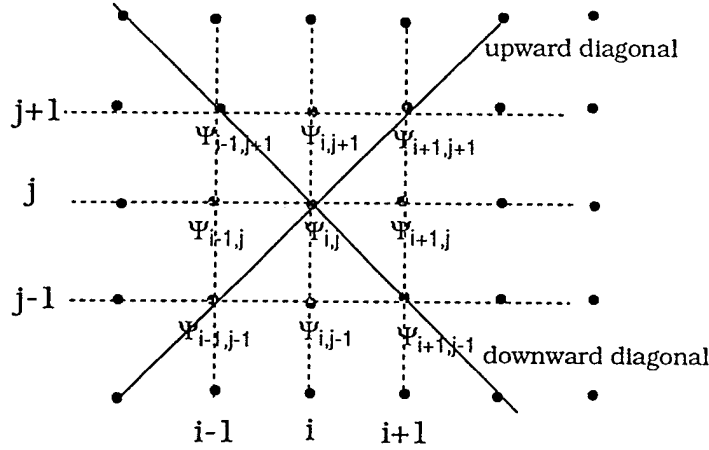


Fig. 1 Field Values Coupled by the ADI Method

As the terms in $M_{xy}\Psi_y$ and $M_{yx}\Psi_x$ along the upward and downward diagonals are decoupled, the ADI may be employed. For the Crank-Nicholson finite difference method, this results in the solution of $2(N_x+N_y)$ pentadiagonal equation systems. Such a procedure is rapid and relatively simple to implement in comparison with sparse matrix inversion techniques.

Results: To illustrate the computational method of the proceeding section, we consider a Y-junction formed from two rib waveguides of height $1.1 \mu\text{m}$ and width $W=2 \mu\text{m}$ etched into a $1.3 \mu\text{m}$ thick epilayer with refractive index $n_1=3.44$. The cladding layer has a refractive index of $n_2=3.34$ while the light wavelength is set to the $\lambda=1.55 \mu\text{m}$. The reference refractive index n_0 is set here to the average of n_1 and n_2 . The refractive index profile of the Y junction is the union of the two waveguide profiles centered at $\pm x(z)$ where $x(z)=2[1-\cos(\pi z/1000\mu\text{m})]$. The computational window dimensions are given by $L_x * L_y = 16 * 8 \mu\text{m}^2$, the number of transverse grid points is $N_x * N_y = 64 * 64$, the propagation step length is $0.1 \mu\text{m}$ and a tapered absorbing region is present over the 8 grid points closest to the computational window boundaries.

In our full vectorial beam propagation analysis, the waveguide is excited with the lowest-order TE mode (Ψ_x, Ψ_y) at the Y-junction input. The intensities of both Ψ_x and Ψ_y along the cross-section located at the at the

etching stop layer is displayed as a function of propagation distance in Figs. 2 and 3, respectively.

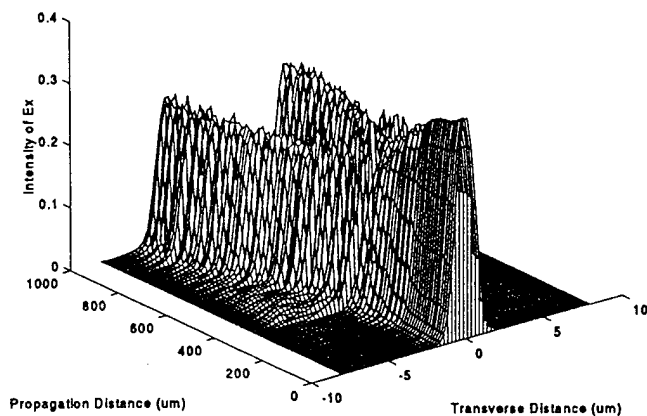


Fig.2 Intensity of Ψ_x along the etching stop layer as a function of propagation distance

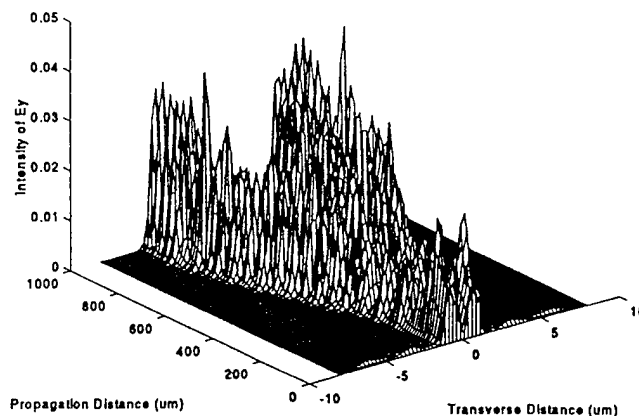


Fig.3 Intensity of Ψ_y along the etching stop layer as a function of propagation distance

We observe from the above figures that the divergence associated with the high-order modes is suppressed by the absorber, as predicted in [5]. Note the periodic transfer of electric field intensity between the TE and TM field components. Calculations performed with the transparent boundary conditions display additional boundary reflections in comparison to the results of the figures.

Conclusions: We have demonstrated a rapid yet accurate alternating directional procedure for the vector wave equation which diverges relatively slowly compared to previous formalisms. Our rib waveguide Y-junction test case indicates that the method is easily stabilized by a properly tailored absorber and thus can be employed to study polarization evolution in a wide variety of components.

Acknowledgments: Support for this work was provided by Bell Northern Research, the Ontario Center for Materials Research, Corning Glass and National Sciences and Research Council of Canada.

Bibliography

- [1] D. Yevick and W. Bardyszewski, "Correspondence of variational finite difference (relaxation) and imaginary distance propagation methods for modal analysis," *Opt. Lett.* vol. 17, pp. 329-330 (1992)
- [2] W. Huang, C. Xu, S. Chu and S. Chaudhuri, "The finite difference vector beam propagation method: analysis and assessment," *J. Lightwave Technol.*, vol. 10, pp. 295-305 (1992)
- [3] P. Liu and B. Li, "Semivectorial beam-propagation method for analyzing polarized modes of rib waveguides," *IEEE J. Quant. Electron.*, vol. 28, pp. 778-782 (1992)
- [4] Y. Chung, N. Dagli and L. Thylen, "Explicit finite difference vectorial beam propagation method," *Electron. Lett.* vol. 27, pp. 21190-2120 (1992)
- [5] D. Yevick, J. Yu, W. Bardyszewski and M. Glasner, "Stability issues in vector field propagation," submitted to *IEEE Photon. Technol. Lett.*
- [6] D. Yevick and M. Glasner, "Forward wide-angle wave propagation in semiconductor rib waveguides," *Opt. Lett.* vol. 15, pp. 174-176 (1990)

Ball lens reflections by direct solution of Maxwell's equations

R. P. Ratowsky , L. Yang¹, R. J. Deri,
J. S. Kallman, and G. Trott¹

Lawrence Livermore National Laboratory
Livermore, California 94551

¹Hewlett-Packard Laboratories
Palo Alto, California 94303-0867

1. Introduction

Ball lenses are important for many applications. For example, ball lenses can be used to match the mode of a laser diode (LD) to a single mode fiber (SMF), essential for low-loss, high bit rate communication systems. Modeling the propagation of LD light through a ball lens presents a challenge due to the large angular divergence of the LD field (typically $> 20^\circ$ HWHM) and the subsequent significant effect of spherical aberration. Accurately calculating the reflected power is also difficult, but essential, since reflections as small as -30 dB can destabilize the LD. [1]

A full-wave analysis of this system using, e.g., a finite-difference time-domain method is not practical because of the size of the ball lens, typically hundreds of wavelengths in diameter. Approximate scalar methods [2] can give good results in some cases, but fail to calculate reflected power and miss polarization effects entirely.

Our approach exploits the fact that the scattering of an arbitrary electromagnetic beam from a sphere is an exactly solvable problem. The scattering of a plane wave from a sphere is a classical problem which was solved by Mie in 1908 [3]. More recently, various workers have considered the scattering of a Gaussian beam from a sphere [4] and its numerical implementation for other applications. To our knowledge, this is the first time this approach has been applied to a problem in optical design. We are able to calculate reflection and transmission accurately with modest computational effort.

2. Method

We assume the ball lens is a perfect, homogeneous sphere, and that departures from ideality can be modeled by a suitable average over lens radius or wavelength. An LD or SMF mode is modeled as an approximately linearly (\hat{x}) polarized (possibly astigmatic) Gaussian beam of vacuum wavelength λ . In the waist plane $z = -z_0$ it has the form

$$E_x(x, y; z = -z_0) = E_0 \exp\left(-\frac{(x - x_0)^2}{\sigma_x^2} - \frac{(y - y_0)^2}{\sigma_y^2}\right),$$

where x_0, y_0 are offsets from the optical (z) axis. We need to know the field everywhere outside the lens, which can be written as the sum of the incident field and a scattered field:

$$\mathbf{E}_{out} = \mathbf{E}_{inc} + \mathbf{E}_{scat}.$$

The scattering problem is solved by a vector multipole expansion of the incident (LD or SMF), scattered and internal fields. Details of this expansion, which involve some subtle convergence issues for wavelength scale LD spot sizes, will be presented at the conference. Satisfying the boundary conditions at the surface of the lens (the continuity of $\hat{r} \times \mathbf{E}$ and $\hat{r} \times \mathbf{H}$) determines the field everywhere. In practice we employ a T-matrix method to calculate the expansion coefficients of the field [3]. We require typically ~1000 terms in the expansion for a convergent result. Once the field is known we can calculate overlap integrals of interest. For example, the power reflected back to an optical fiber is $R = \iint \mathbf{E}_{inc}^* \cdot \mathbf{E}_{scat} dx dy$, where the integral is over the plane of incidence $z = -z_0$.

3. Results

To validate our method, we have calculated the back reflection to a SMF of mode size $4.5 \mu\text{m}$ (half-width at $1/e^2$ intensity) at various lens-fiber distances for two different ball lenses: $250 \mu\text{m}$ sapphire ($n = 1.75$) and $300 \mu\text{m}$ BK-7 ($n = 1.5$). In all cases the fiber is on the optical axis. The light wavelength is $1.3 \mu\text{m}$. The back reflections were also measured experimentally. These results are shown in Fig. 1; it is apparent that the calculation agrees with experiment in most cases to better than 1 dB.

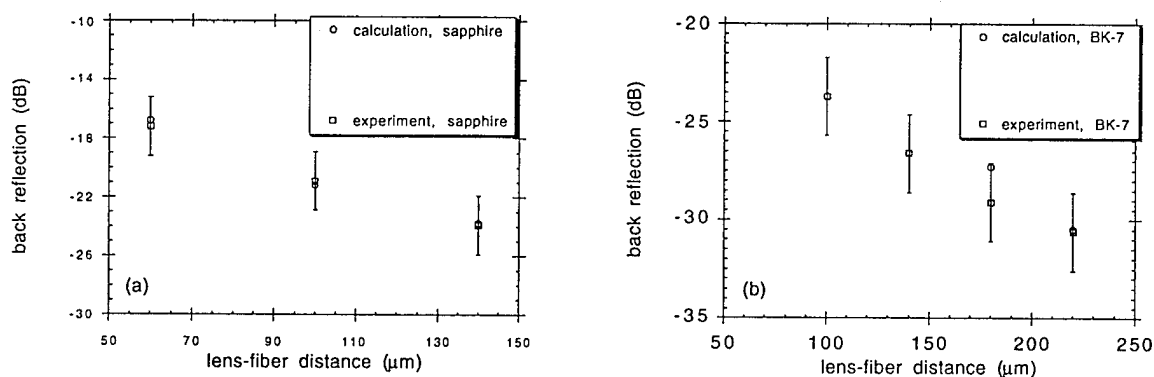


Fig. 1. (a) Back reflection to SMF from (a) 250 mm radius sapphire lens; (b) 300 mm radius BK-7 lens

The SMF results give us confidence to calculate the back reflection to an LD, where measurements are much more difficult to make. In Fig. 2 we show the back reflection to an LD of symmetric spot size $(0.85 \mu\text{m} \times 1.22 \mu\text{m})^2$ as the LD-lens distance is varied. For comparison, we also show the result obtained from a symmetric $(1.22 \mu\text{m})^2$ spot. Note the nonmonotonic behavior, probably due to high-order resonances in the spherical lens.

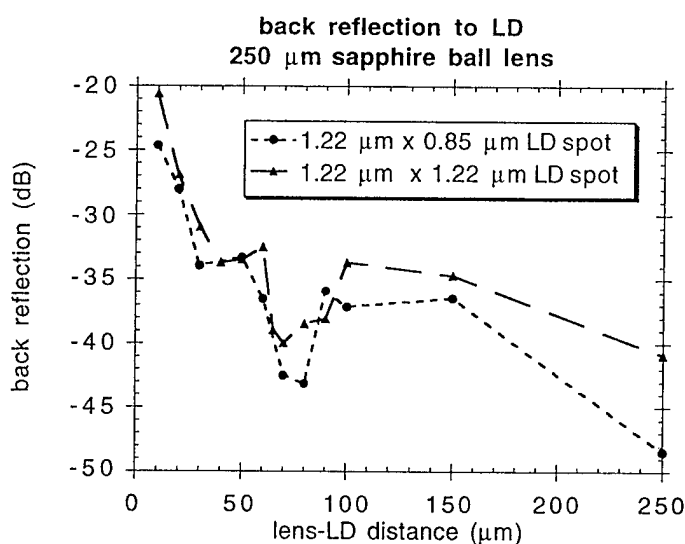


Fig. 2 Back reflected power to a LD for a 300 mm radius ball lens.

Our results clearly indicate that we are able to predict accurately the reflection from a ball lens to a SMF. We believe our method can accurately predict the back reflection for the LD, which is very difficult to make reliably using any other existing method. This technique will additionally allow us to study the effect of misalignments, and the extension of the method to antireflection coated lenses is straightforward. Calculations of coupling to optical fibers will also be forthcoming.

Acknowledgments

We are grateful to Dr. E. Khaled and Dr. S. Hill for making their code available to us and for helpful advice. We thank Dr. M. Pocha and Dr. K. Carey for useful discussions. This work was performed in part under the auspices of the U. S. Department of Energy by the Lawrence Livermore National Laboratory under contract No. W-740-ENG-48.

References

- [1] H. Temkin, N. A. Olsson, J. H. Abeles, R. A. Logan and M. B. Panish, IEEE J. of Quantum Electronics, Vol. QE-22, No. 2, 1986.
- [2] H. Karstensen, J. Opt. Comm. 9 (1988) 2, 42.
- [3] G. Mie, Ann. Physik 25, 377 (1908); H.C. van de Hulst, "Light Scattering by Small Particles" (Dover, New York, 1957).
- [4] E. E. M. Khaled, Ph.D. diss. (Dept. of Electrical and Computer Engineering, Clarkson University, Potsdam, NY, 1992); E. E. M. Khaled, S. C. Hill and P. W. Barber, IEEE Trans. Antennas Propag. 41, 295 (1993).

summary

We calculate reflection from ball lenses by exactly solving Maxwell's equations for the scattering of a beam from a dielectric sphere. Our results are validated by experiment.

IPR KEY TO AUTHORS

Amersfoort, M. R.	- PD3
Andreadakis, N. C.	- PD3
Aronson, L. B.	- PD6
Baran, Jane E.	- PD5
Bardyszewski, Witold	- PD8
Caneau, C.	- PD3
Centanni, J. C.	- PD2
Chakravarthy, Rohini S.	- PD5
Dasler, Marie	- PD4
Deri, R. J.	- PD9
Di Giuseppe, N. J.	- PD1
Dolfi, D. W.	- PD6
Forrest, S. R.	- PD1
Fritz, Daniel J.	- PD5
Hirono, T.	- PD7
Jackel, Janet Lehr	- PD5
Joyner, C. H.	- PD2
Kallman, J. S.	- PD9
Kim, D. S.	- PD1
Lange, M. J.	- PD1
LeBlanc, H. P.	- PD3
Martinelli, R. U.	- PD1
Olsen, G. H.	- PD1
Oohashi, H.	- PD7
Rajhel, A.	- PD3
Ranganath, T. R.	- PD6
Rankin, G.	- PD6
Ratowsky, R. P.	- PD9
Seki, S.	- PD7
Smith, David A.	- PD5
Soole, J. B. D.	- PD3
Stoltz, Bjorn	- PD4
Sugiura, H.	- PD7
Trott, G.	- PD9
Weber, Jean-Pierre	- PD4
Yang, L.	- PD9
Yevick, David	- PD8
Yokoyama, K.	- PD7
Yu, Jun	- PD8
Zirngibl, M.	- PD2